Monthly Notices of the ROYAL ASTRONOMICAL SOCIETY

MNRAS **538,** 3001–3022 (2025) https://doi.org/10.1093/mnras/staf416
Advance Access publication 2025 March 13

ALMA observations of dual quasars: evidence of rich and diverse molecular gas environments

Shenli Tang [1,2,3★] John D. Silverman,[3,4,5,6] Zhaoxuan Liu,[3,4] Manda Banerji [1] Tomoko Suzuki [4] Seiji Fujimoto [7] Andy Goulding,[8] Masatoshi Imanishi [9] Toshihiro Kawaguchi,[10] Connor Bottrell [2,11] Tilman Hartwig [12,13] Knud Jahnke [14] Masafusa Onoue,[2,15] Malte Schramm[16] and Yoshihiro Ueda[17]

[1]*School of Physics & Astronomy, University of Southampton, Highfield Campus, Southampton SO17 1BJ, UK*
[2]*Department of Physics, University of Tokyo, Tokyo 113-0033, Japan*
[3]*Kavli Institute for the Physics and Mathematics of the Universe (WPI), The University of Tokyo, Kashiwa, Chiba 277-8583, Japan*
[4]*Department of Astronomy, School of Science, The University of Tokyo, 7-3-1 Hongo, Bunkyo, Tokyo 113-0033, Japan*
[5]*Center for Data-Driven Discovery, Kavli IPMU (WPI), UTIAS, The University of Tokyo, Kashiwa, Chiba 277-8583, Japan*
[6]*Center for Astrophysical Sciences, Department of Physics & Astronomy, Johns Hopkins University, Baltimore, MD 21218, USA*
[7]*Department of Astronomy, The University of Texas at Austin, Austin, TX 78712, USA*
[8]*Department of Astrophysics, Princeton University, Princeton, NJ 08544, USA*
[9]*National Astronomical Observatory of Japan, 2-21-1 Osawa, Mitaka, Tokyo 181-8588, Japan*
[10]*Department of Economics, Management and Information Science, Onomichi City University, Hisayamada 1600-2, Onomichi, Hiroshima 722-8506, Japan*
[11]*International Centre for Radio Astronomy Research, University of Western Australia, 35 Stirling Highway, Crawley, WA 6009, Australia*
[12]*Institute for Physics of Intelligence, The University of Tokyo, 7-3-1 Hongo, Bunkyo, Tokyo 113-0033, Japan*
[13]*Application Lab for AI and Big Data, German Environment Agency, Alte Messe 6, 04103 Leipzig, Germany*
[14]*Max-Planck-Institut für Astronomie, Königstuhl 17, 69117 Heidelberg, Germany*
[15]*Kavli Institute for Astronomy and Astrophysics, Peking University, Beijing 100871, China*
[16]*Graduate school of Science and Engineering, Saitama University, 255 Shimo-Okubo, Sakura-ku, Saitama City, Saitama 338-8570, Japan*
[17]*Department of Astronomy, Kyoto University, Kitashirakawa-Oiwake-cho, Sakyo-ku, Kyoto 606-8502, Japan*

Accepted 2025 March 6. Received 2025 March 3; in original form 2024 July 15

ABSTRACT

We present a study of the molecular gas in five closely separated ($R_\perp < 20$ kpc) dual quasars ($L_{\rm bol} \gtrsim 10^{44}$ erg s^{-1}) at redshifts $0.4 < z < 0.8$ with the Atacama Large Millimeter/submillimeter Array. The dual quasar phase represents a distinctive stage during the interaction between two galaxies for investigating quasar fueling and feedback effects on the gas reservoir. The dual quasars were selected from the Sloan Digital Sky Survey and Subaru/Hyper Suprime-Cam Subaru Strategic Programme, with confirmatory spectroscopic validation. Based on the detection of the CO J = 2–1 emission line with Band 4, we derive key properties including CO luminosities, line widths, and molecular gas masses for these systems. Eight quasars, of the 10 in pairs, have line detections exceeding 5σ that result in molecular gas masses ($M_{\rm molgas}$) between $10^{9.7-10.7}$ M$_\odot$. The molecular gas-to-stellar mass ratios ($\mu_{\rm molgas}$) of these dual quasars are typically between 18–50 per cent, which are similar to the single quasars in mergers and inactive star-forming galaxies. The results indicate no clear evidence of molecular gas depletion attributed to dual quasar activities on global scale. However, intriguing gas features in certain systems appear to show possible signatures of active galactic nucleus (AGN) feedback effect.

Key words: molecular data – galaxies: active – galaxies: interactions – quasars: emission lines.

1 INTRODUCTION

Quasar activity is frequently linked to the hierarchical growth of galaxies. During galaxy collisions, the significant interaction can ignite star formation and potentially quicken the growth of their central supermassive black holes (SMBHs) (e.g. Sanders & Mirabel 1996; Hopkins et al. 2006). These interactions might explain the observed correlations between SMBHs' physical properties and those of their host galaxies (e.g. Di Matteo, Springel & Hernquist 2005; Di Matteo et al. 2008). When both merging galaxies contain an SMBH, it can initiate a phase where both are simultaneously active, resulting in a dual quasar. The detection of dual quasars, initially observed at separations of several arcseconds, was first documented by Owen et al. (1985) and gained traction through the Sloan Digital Sky Survey (SDSS) (Hennawi et al. 2006, 2010). Nevertheless, identifying dual quasars with separations of $\lesssim$20 kpc beyond the nearby Universe has been difficult due to resolution limitations, which require both sources to be distinguishable to confirm their separate nuclei. Fig. 1 presents a collection of dual quasars confirmed using optical spectroscopy, X-ray, or radio emission (see also Chen et al. 2022). This includes nearly identical quasars (NIQs) identified

★ E-mail: st1c23@soton.ac.uk

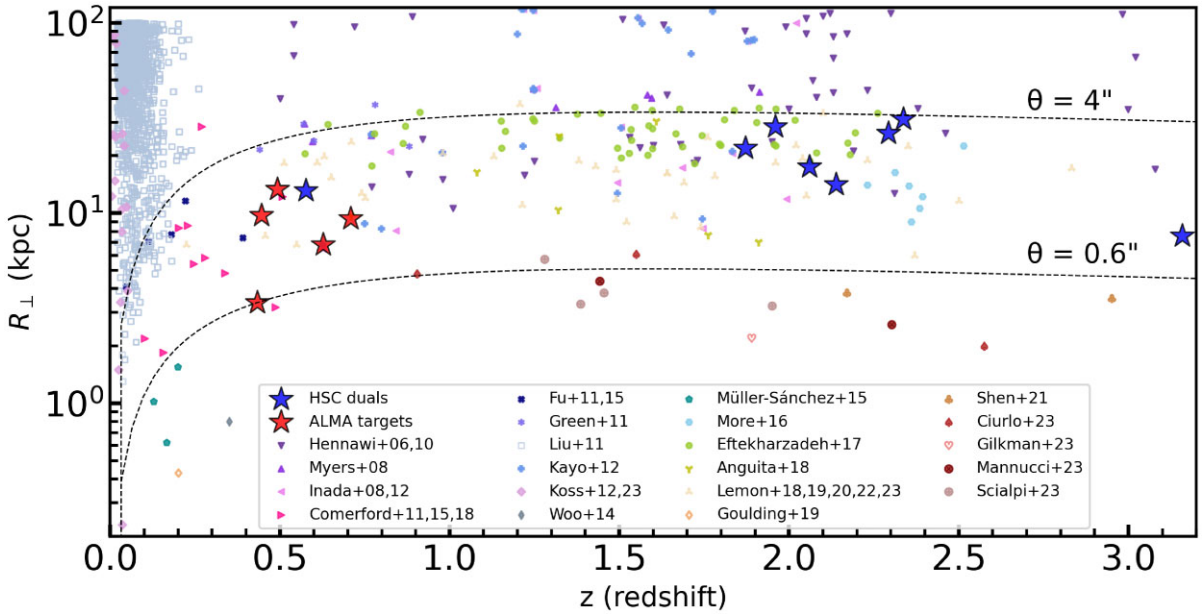

Figure 1. Dual quasar ensemble plotted with projected physical separation ($R_\perp$ in kpc) against redshift. Dual quasars validated via our HSC initiative are illustrated in red for the five ALMA targets, while others appear in blue (Tang et al., in preparation). Dual quasars confirmed through spectroscopy from prior studies are also represented (Hennawi et al. 2006, 2010; Inada et al. 2008, 2012; Myers et al. 2008; Comerford et al. 2011, 2015, 2018; Fu et al. 2011, 2015; Green et al. 2011; Liu et al. 2011; Kayo & Oguri 2012; Koss et al. 2012, 2023; Woo et al. 2014; Müller-Sánchez et al. 2015; More et al. 2016; Eftekharzadeh et al. 2017; Anguita et al. 2018; Lemon et al. 2018, 2019, 2020, 2022, 2023; Goulding et al. 2019; Shen et al. 2021; Ciurlo et al. 2023; Glikman et al. 2023; Mannucci et al. 2023; Scialpi et al. 2023). Dashed lines delineate the selection zone spanning 0.6 arcsec–4 arcsec for our HSC study. Specifically, the ALMA targets are positioned within 0.6 arcsec–2.2 arcsec.

in lens surveys, recognized as quasar pairs with similar spectra but lacking photometric evidence of a lens galaxy (Anguita et al. 2018; Lemon et al. 2018; Lemon, Auger & McMahon 2019; Lemon et al. 2020). The highest redshift dual quasars have been reported up to z = 5.66 (Yue et al. 2021b) and z = 6.05 (Matsuoka et al. 2024). Their spatial separations can reach down to 430 pc (Goulding et al. 2019) and 230 pc (Koss et al. 2023). This variation in redshifts and separations of dual quasars showcases their presence at various merger phases of galaxies throughout cosmic history.

The study of dual quasar systems has sparked simulation endeavours to explore both their frequency and intricate dynamics within galaxy interactions. Hydrodynamic cosmological simulations have estimated the 'dual fraction' – the ratio of dual quasars to all quasars – to vary from several thousandths to a few per cent (Van Wassenhove et al. 2012; Steinborn et al. 2016). Some research further suggests that this fraction increases with redshift (Volonteri et al. 2016; Rosas-Guevara et al. 2019; Volonteri et al. 2022). Concurrently, numerical simulations have examined the evolving physical characteristics of dual quasars and their host galaxies as they merge (Capelo et al. 2015, 2017). Hence, the pursuit of dual quasars at smaller separations and their further study using multiwavelength observations are of great importance. These efforts intend to validate these simulations and shed light on the fundamental physics controlling their co-evolutionary processes (see review by De Rosa et al. 2019).

Research has progressed on the host galaxies of dual quasars, despite the limitations primarily due to small sample sizes and the challenge of distinguishing quasar light from host galaxy light in low-resolution data, particularly for those beyond the nearby galaxies. A viable technique involves 2D modelling of high-quality images. For instance, Chen et al. (2023) investigated the dual quasar SDSS J0749+2255, located at $z = 2.17$ and separated by 3.8 kpc, through observations with the *Hubble Space Telescope* (*HST*). They discovered that the quasar resides in massive, compact disc-dominated galaxies exhibiting tidal features. This finding serves as clear evidence of active interactions within dual quasars, potentially developing into compact, gravitationally bound binary supermassive black holes (SMBHs). More recently, the *JWST* has demonstrated its capability to illuminate the 3D structure of such systems (Chen et al. 2024; Ishikawa et al. 2024) and to validate similar candidates in different settings (Maiolino et al. 2023; Perna et al. 2023; Li, Zhuang & Shen 2024; Übler et al. 2024).

Ground-based telescopes, on the other hand, provide benefits in terms of efficiency and cost when performing systematic surveys. Since our initial publication (Silverman et al. 2020), we have embarked on a search for dual quasars within the Subaru Hyper Suprime-Cam Subaru Strategic Program (HSC/SSP) area, focusing on those with close separations (0.6 arcsec–4 arcsec, as indicated by the dashed lines in Fig. 1). The selection of candidates involves assessing morphology and colour, followed by detailed multiwavelength spectroscopic evaluations to confirm their nature and explore their physical characteristics. In Silverman et al. (2020), we spectroscopically confirmed three dual quasars using Keck/LRIS. Following this, Tang et al. (2021) reported three more confirmed dual quasars discovered via Gemini-GMOS and Subaru/FOCAS. Using optical spectroscopy and imaging, we determined their black hole and host properties. So far, we have focused on investigating the stellar contents of their host galaxies, with the properties of their gas and dust still unexamined.

Comprehensive studies on molecular gas have been carried out across diverse galaxy groups, including individual quasar host galaxies. Xia et al. (2012) employed the 30-meter IRAM telescope to examine 19 infrared ultraluminous quasars at $z < 0.4$, detecting the CO J = 1–0 emission line in 17 cases, and revealing molecular gas content akin to ULIRGs ($M_{\rm molgas} \sim 10^{9-10}\,{\rm M}_\odot$). Similar observations

have been documented by Krips, Neri & Cox (2012) and Husemann et al. (2017). Shangguan et al. (2020) utilized the Atacama Large Millimeter/submillimeter Array (ALMA) to explore CO J = 2–1 emission in 23 Palomar-Green (PG) quasars at $z < 0.1$, finding a 91 per cent detection rate with an average molecular gas mass of $10^{9.20\pm0.13}M_{\odot}$ for their quasar host galaxies, comparable to inactive galaxies of equivalent stellar mass. A lack of relationships between quasar properties and overall CO characteristics is also noted in $z < 0.5$ PG quasars (Molina et al. 2023) and $z < 0.2$ type 2 quasars (Molyneux et al. 2024). Conversely, Izumi et al. (2020) observed 4 quasars and 4 comparable inactive star-forming galaxies (SFGs) at $z < 0.06$, discovering greater molecular gas surface densities in SFGs compared to quasars on scales smaller than 500 pc. Consequently, these low-z findings appear to support a merely 'local' (e.g. circumnuclear-scale) influence of active galactic nucleus (AGN) feedback on the molecular gas. On the other hand, ALMA has substantially enhanced quasar studies during the epoch of reionization (Wang et al. 2013; Decarli et al. 2017; Jones et al. 2017; Shao et al. 2017; Venemans et al. 2017; Willott, Bergeron & Omont 2017; Izumi et al. 2018; Nguyen et al. 2020; Yue et al. 2021a; Walter et al. 2022) and at cosmic noon (Banerji et al. 2017, 2021; Schulze et al. 2019; Scholtz et al. 2023). Intriguingly, these examinations generally indicate a relatively diminished gas environment around quasar hosts. This variation might be attributed to the rising luminosities of quasars in the early Universe (Shen et al. 2020), suggesting that higher-z quasars might display more effective feedback to diminish their gaseous surroundings (Valentini et al. 2020). Differences may also stem from increased obscuration and merger rates in high-redshift quasars (Treister et al. 2010). Thus, a fair comparison needs a carefully controlled framework that considers all these elements.

Concerning the dual quasars analysed in this study, they represent distinct merger events, supported by both spectroscopic and photometric data. These samples have redshifts ranging from 0.4 to 0.8, effectively linking the local Universe with the cosmic noon. These five dual quasars serve as an exemplary initial sample for examining the influence of quasar feedback on the molecular gas environment within a clearly defined context. There is a lack of comprehensive observations regarding molecular gas in dual quasars within this redshift range documented in the literature. In this study, we broaden our research scope by observing the CO J = 2–1 emission from the five dual quasars using ALMA Band 4, in order to evaluate the molecular gas content in their host galaxies. This study seeks to address two central questions: (1) With the concurrent activation of two quasars, does the molecular gas in dual quasars become more depleted compared to that in single quasars and inactive star-forming galaxies? (2) Are there distinct spatial distributions and kinematic structures of the molecular gas within each pair?

The structure of the paper is organized as follows: Section 2 outlines our sample selection, the set-up for observations, and the data reduction process. Section 3 describes the comprehensive measurements of the observed CO properties along with the deduced gas characteristics, which is then followed by the specific details highlighting the notable attributes of each pair. Section 4 provides a comparison of the CO properties of dual quasars with those of single quasars and inactive galaxies from the existing literature, examining whether these systems have undergone quenching. Additionally, we explore the implications regarding the linkages between galaxy mergers and quasar activity as derived from our findings. This study uses a lambda cold dark matter (ΛCDM) cosmology with parameters $\Omega_{\Lambda} = 0.7$, $\Omega_{\rm m} = 0.3$, and $H_0 = 70$ km s^{-1}Mpc^{-1}.

2 METHODS

2.1 Sample selection

Our selection of dual quasars originates from the SDSS DR14 quasar catalogue (Pâris et al. 2018), captured within the Subaru HSC/SSP PDR3 footprint (Aihara et al. 2022). Using the 2D image modelling tool GALIGHT (Ding et al. 2022), we selected quasars accompanied by another nearby point source with a separation of 0.6–4 arcsec. These quasars typically span redshifts from 0 to 4, with bolometric luminosities that typically exceed 10^{44} erg s^{-1}.

The validation process involved spectroscopic observations to confirm the nature of companion sources. Here, confirmation of a dual quasar requires the detection of a broad emission line in both sources, with the line centre being offset by at most 2000 km s^{-1} following Hennawi et al. (2006). To date, we have confirmed 13 dual quasars (Tang et al. in preparation), as denoted by the star marks in Fig. 1. Among the five dual quasars targeted for ALMA observation in this study, highlighted in red, four belong to unobscured (type1–type1) quasar pairs, while one constitutes a partly obscured-unobscured pair (type1–type1.5). The angular separations of these five dual quasars span 0.6–2.2 arcsec, translating into projected physical separations ranging from 3.9–13.3 kpc. This sample enables investigations of the molecular gas content and dynamics during a phase approximately 200 million years prior to the final coalescence of a galaxy merger, as expected from numerical simulations. (Capelo et al. 2015, 2017).

In the following texts, we will refer to these five dual quasars by their abbreviated names: J0847, J1214, J1416, J2209, and J2237 in the subsequent content, corresponding to their SDSS J2000 designations.

2.2 Optical/near-Infrared photometry

We first present our analysis on the optical/near-infrared photometry of these five systems to decide their stellar masses, which are essential for the estimation of the molecular gas-to-stellar mass ratio ($\mu_{\rm molgas}$).

As detailed in Section 2.1, the imaging analysis tool GALIGHT is utilized for identifying dual quasar candidates. Concurrently, it locates the nucleus centres and estimates the host galaxies' magnitudes after subtracting the point source contributions across all five bands. In this study, we refine the fitting approach as outlined in Silverman et al. (2020) and Tang et al. (2021) using the version 0.2.1 of GALIGHT (Ding et al. 2022). Related methods have been applied in Tang et al. (2023) and Ding et al. (2023) employing the same tool. Essentially, the tool conducts a two-dimensional fit using point spread functions (PSFs) for the quasars and applying Sérsic profiles for the galaxies. We acquire the PSF models for each dual quasar in every band from the HSC PSF picker tool,[1] located at the position of one of the quasars. This PSF model is produced by the HSC image processing system (Bosch et al. 2018), derived from an adapted version of the PSFEX software (Bertin 2013). The amplitude and sky position of the PSF are used as variable parameters. Additionally, the Sérsicprofiles have the Sérsicradius, index, and ellipticity as variable parameters. The initial positions and apertures of the model are determined by the PHOTUTILS package's source detection algorithm (Bradley et al. 2024). We start by fitting the i-band image, which provides the highest image quality among the bands (Aihara et al. 2022). Subsequently, the results from i-band are used as initial parameter configurations for the remaining four bands.

[1] https://hscdata.mtk.nao.ac.jp/psf/9/

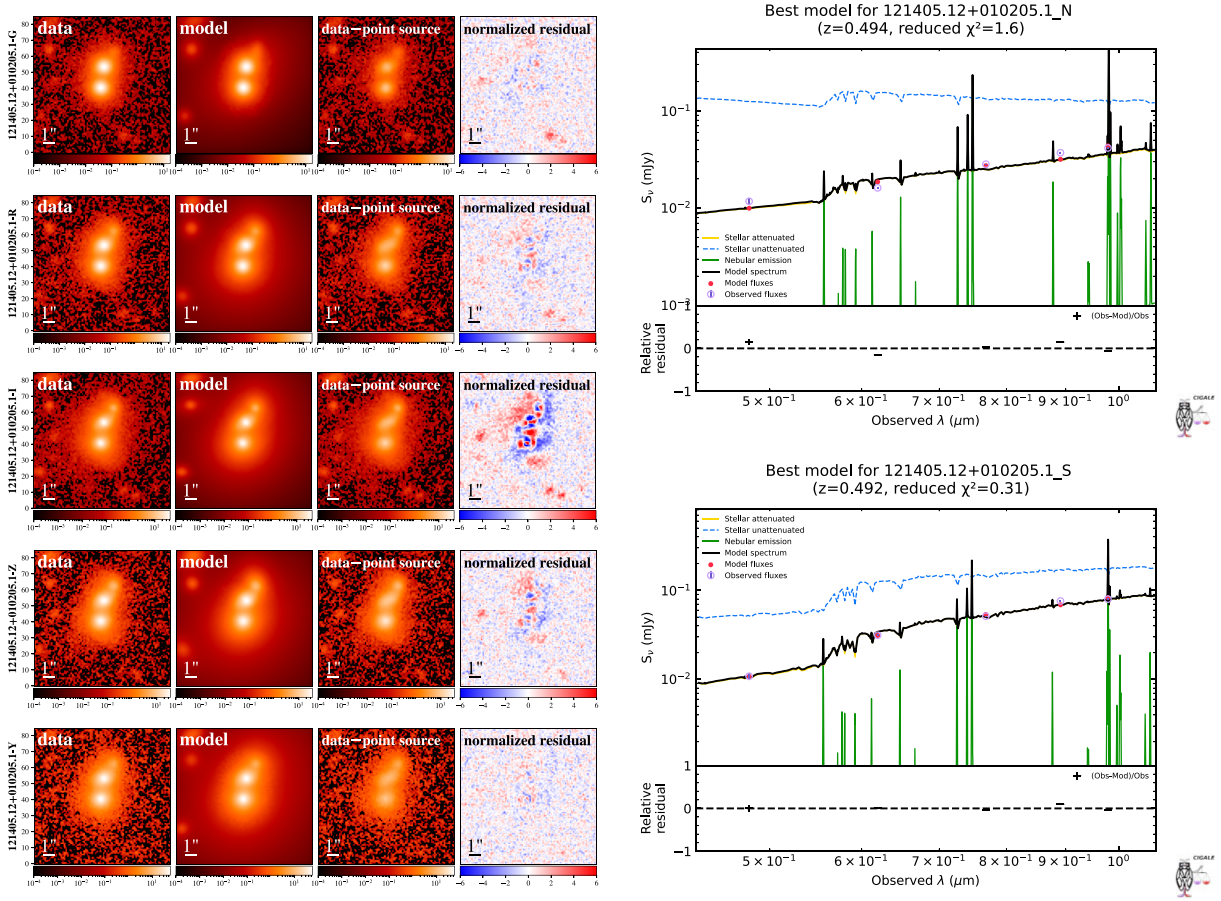

Figure 2. Photometric evaluations conducted with GALIGHT and CIGALE on J1214. Left: 2D image analysis using GALIGHT on the five-band HSC data for this system. Right: Spectral energy distribution (SED) fits for J1214N (at the top) and J1214S (at the bottom) utilizing CIGALE. Further details are described in Section 2.2. The results of all the five pairs are provided in the online supplementary material.

The optimal fit results for J1214 using GALIGHT are illustrated in the left panels of Fig. 2, as an example. From top to bottom, results are displayed for the g, r, i, z, and y bands. Each row contains the following, from left to right: (1) the original HSC image of the dual quasar, (2) the optimal model of the system incorporating two PSF models along with several Sérsiccomponents modelling both the host galaxies and the surrounding sources, (3) the galaxy image after removal of the PSF models, (4) a normalized residual map – calculated as (data–model)/noise.

For each system, we perform the fitting process twice: once using the particle swarm optimization (PSO, Kennedy & Eberhart 1995) approach to minimize the loss function, and once employing the Markov Chain Monte Carlo (MCMC, Gilks, Richardson & Spiegelhalter 1995) method to maximize the likelihood function. In Table 1, columns (2)–(6) display the MCMC-derived five-band magnitudes for the host galaxies associated with each quasar. For J0847 and J1416, the fitting apertures imply that each pair of quasar components shares the same host galaxy, resulting in a single reported value for each. From 10 000 MCMC samplers, the majority of cases show 1σ uncertainties below 0.1 mag, while for J2337N, they range from 0.1 to 0.4 mag across different bands. Upon comparison, the discrepancies between the MCMC and PSO outcomes are generally within 1σ uncertainty of MCMC, with just two instances showing 1–2σ differences.

Afterward, we determine the galaxy flux fraction ($f_{\rm gal}$) for each system as:

$$f_{\rm gal} = F_{\rm gal}/(F_{\rm gal} + F_{\rm qso}) \quad (1)$$

where $F_{\rm gal}$ refers to the flux of the host galaxy, and $F_{\rm qso}$ to the flux of the quasar, derived from the optimal model fit. For J0847 and J1416, $F_{\rm qso}$ includes contributions from two quasars. The $f_{\rm gal}$ values are detailed in columns (7)–(11) of Table 1.

Utilizing these flux measurements, we perform spectral energy distribution (SED) fitting with the tool Code Investigating GALaxy Emission (CIGALE; Boquien et al. 2019). An illustration for J1214 can be seen in Fig. 2 right panels. The top panel illustrates the results for J1214N, while the bottom is for J1214S. The observed magnitudes are translated to mJy and shown as purple open circles with accompanying error bars. The red filled circles and black line denote the best-fitting SED model. This model integrates a delayed star formation history (SFH) and stellar assembly (Bruzual & Charlot 2003; Maraston 2005), alongside dust attenuation (Calzetti et al. 2000; Charlot & Fall 2000), re-emission (Dale et al. 2014), and nebular emission (Inoue 2011), represented by the coloured lines. Throughout our fitting, we use the Chabrier (2003) initial mass function (IMF). The lower sub-plot illustrates the relative residuals, specifically (data-model)/data. In total, CIGALE computes 40 950

Table 1. Photometric evaluations of the host galaxies for the dual quasars with GALIGHT and CIGALE. Column (1) Abbreviated names of the sources, the full SDSS J2000 name of the sources can be found in Table 2. The pair of J0847 and J1416 share one single host galaxy per each, so their respective measurements are consolidated. Columns (2)–(6) present the magnitudes of these host galaxies across five bands after point sources have been extracted in HSC. Based on the distribution from 10 000 MCMC samplers, most uncertainties are less than 0.1 mag. For J2337N, the uncertainties are estimated as 0.4, 0.3, 0.1, 0.1, 0.2 mag in the g, r, i, z, and y bands, respectively. Columns (7)–(11) detail the flux fractions of the galaxies in the observed-frame across five bands, represented as $f_{\rm gal} = F_{\rm gal}/(F_{\rm gal} + F_{\rm qso})$. The stellar mass identified from the optimal CIGALE model using the five-band photometry is given in Column (12).

Name	$m^g_{\rm gal}$ (mag)	$m^r_{\rm gal}$ (mag)	$m^i_{\rm gal}$ (mag)	$m^z_{\rm gal}$ (mag)	$m^y_{\rm gal}$ (mag)	$f^g_{\rm gal}$ (%)	$f^r_{\rm gal}$ (%)	$f^i_{\rm gal}$ (%)	$f^z_{\rm gal}$ (%)	$f^y_{\rm gal}$ (%)	log M_* ($M_\odot$)
(1)	(2)	(3)	(4)	(5)	(6)	(7)	(8)	(9)	(10)	(11)	(12)
J0847	20.8	19.8	19.3	19.2	19.0	20.2 ± 0.4	33.6 ± 0.3	35.7 ± 0.1	40.1 ± 0.2	40.9 ± 0.5	10.95 ± 0.16
J1214N	21.2	20.9	20.3	20.0	19.9	33.1 ± 2.3	37.9 ± 0.7	46.9 ± 0.4	52.5 ± 1.3	35.5 ± 0.9	10.08 ± 0.28
J1214S	21.2	20.2	19.6	19.2	19.1	31.0 ± 2.3	63.4 ± 1.2	69.1 ± 0.7	83.2 ± 1.9	52.5 ± 1.4	10.85 ± 0.15
J1416	20.4	19.3	18.7	18.4	18.0	39.9 ± 0.5	58.8 ± 0.4	64.3 ± 0.2	63.6 ± 0.4	63.8 ± 0.7	11.19 ± 0.13
J2209N	22.2	21.0	20.3	20.1	20.2	19.8 ± 1.1	41.5 ± 0.9	54.0 ± 0.7	53.0 ± 0.9	34.4 ± 1.1	10.28 ± 0.16
J2209S	21.8	20.7	20.2	19.8	19.6	48.5 ± 1.8	61.4 ± 1.2	70.1 ± 0.8	71.3 ± 1.7	64.7 ± 3.0	10.62 ± 0.14
J2337N	25.1	23.3	21.1	21.4	21.4	1.6 ± 0.5	6.6 ± 1.5	25.8 ± 1.6	23.9 ± 2.6	23.5 ± 3.7	10.60 ± 0.22
J2337S	21.6	21.2	20.0	19.6	19.4	20.0 ± 0.6	22.0 ± 0.5	39.1 ± 1.7	49.9 ± 1.4	55.6 ± 2.0	11.34 ± 0.14

Table 2. ALMA observation setups for the dual quasars. Columns (2)–(4): optical position and redshift of the SDSS quasar in the pair. See Table A1 for reanalysed values on both sources. (5) Sensitivity of the emission line in 10 km s^{-1} width. (6) Restored beam size with natural weighting (Briggs 2.0) (7) Minimum velocity resolution. (8) Precipitable water vapor. (10) Total integration time in seconds.

Name (SDSS J2000)	RA (deg)	Dec. (deg)	z	Line sens. (mJy beam^{-1})	Beam size (arcsec^2)	R_v (km s^{-1})	PWV (mm)	Humidity (%)	$t_{\rm int}$ (s)	Date (yy-mm-dd)
(1)	(2)	(3)	(4)	(5)	(6)	(7)	(8)	(9)	(10)	(11)
084 710.40–001 302.6	131.793 36	0.217 41	0.6269	0.595	0.89×0.76	8.287	0.42	7.87	1603	22-06-10
121 405.12+010 205.1	183.521 36	1.034 78	0.4927	0.664	0.86×0.81	7.611	2.04	28.35	1300	22-01-07
141 637.44+003 352.2	214.156 02	0.564 52	0.4336	0.559	0.33×0.24	7.331	1.16	7.49	2480	21-11-28
220 906.91+004 543.9	332.278 81	0.762 19	0.4461	0.679	0.91×0.68	7.374	1.92	8.90	1360	21-12-30
233 713.66+005 610.8	354.306 95	0.936 34	0.7078	0.574	0.54×0.51	8.003	4.75	30.63	1814	21-12-05

models to match each source. The reduced χ^2 for the optimal model is indicated by the panel title. In five out of the eight measurements, the reduced χ^2 values are below 1. The case of J2337N shows the highest reduced χ^2 of 4.4. The calculated total stellar mass (M_*) is presented in column (12) of Table 1. The GALIGHT and CIGALE fitting results of all five pairs are provided as supplementary material for this study, together with the initial parameter configuration file for CIGALE.

2.3 ALMA observation and data analysis

2.3.1 The ALMA observation

We carried out our observations during ALMA Cycle 8, which ran from 2021 November to 2022 June (Project ID: 2021.1.01233.S, PI: Tang). These observations involved mapping the CO J = 2–1 emission using setups with 41 to 48 12-meter antennas equipped with Band 4 receivers. The 1.875 GHz bandpass was segmented into 480 spectral channels, each with an averaging factor of 8, culminating in a spectral resolution of 3904 kHz. This resolution translates to an approximate velocity resolution of around 8 km s^{-1} at the observed frequency. The overall frequency coverage, spanning 4 spectral windows across two sidebands, was 7.5 GHz in total. The observational configurations, parameters, and weather data can be found in Table 2.

For data reduction, we employed CASA version 6.4.1 (Bean et al. 2022) using the Measurement Set (MS) files provided. Each MS file, obtained from the raw observations, is calibrated via the auxiliary file 'scriptForPI.py,' hence it is termed as the 'calibrated visibility.' For each specific source, a full array of calibrators–including those for atmosphere, bandpass, flux, phase, pointing, and water vapour radiometers (WVR) – is applied. Further details of this calibration process are available in the ALMA Science Pipeline User's Guide,[2] along with QA reports in the ALMA project repository.

2.3.2 CO measurements

Starting with the MS file, our first task was to divide the visibility into emission line and continuum windows using the SPLIT task. The only emission line detected by our setup is CO J = 2–1. To pinpoint this line, we performed a preliminary spectral profile fitting by using the Cube Analysis and Rendering Tool for Astronomy (CARTA v4.1; Comrie et al. 2021) on the science products. We flag channels within $\pm 5 \times$ FWHM of the line, designating those outside this range as continuum channels. The TCLEAN task in multifrequency synthesis mode (`mfs`) is then employed to create the continuum map. To capture possible extended data structures, we use the `Multiscale` deconvolver (Cornwell 2008). For Briggs weighting (Briggs 1995), the robustness parameter (R) is set to 2 (natural weighting), enhancing sensitivity. However, the continuum remains undetected in all sources, with 3σ upper limits around $\sim$ 40 μJy (see the bottom row of Fig. 3). For the emission line, we also investigate using R = 0.5, observing peak flux differences from R = 2 of no more than 15 per cent. Other parameters remain at their defaults. We subsequently employ the TCLEAN task, preserving the

[2]https://almascience.nrao.edu/processing/science-pipeline

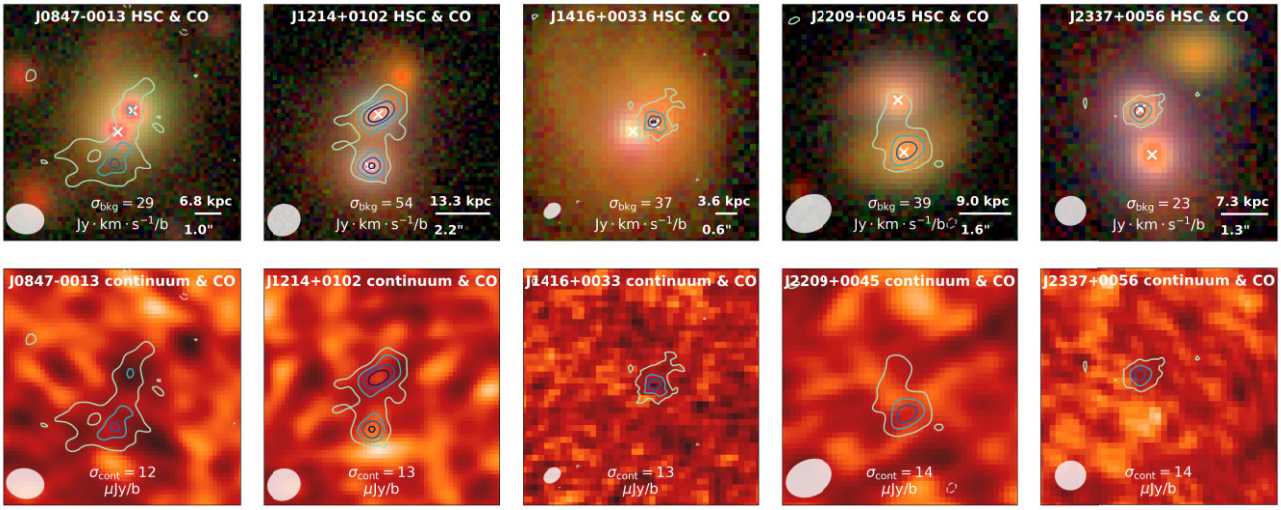

Figure 3. Top row: HSC (*gri* bands) images of five dual quasars displayed with the contours of the CO J = 2–1 emission line M0 map superimposed. The ALMA beam size is illustrated by a white ellipse located at the bottom left corner. The background noise level ($\sigma_{\rm bkg}$) is derived from the residual maps and is indicated at the base of each panel. Positive contours commence at $3\sigma_{\rm bkg}$ and move upward by increments of $3\sigma_{\rm bkg}$. A limited number of negative $3\sigma_{\rm bkg}$ contours are shown with white dashed lines. The optical centres of the point sources are marked with white crosses, and the scale bar at the bottom right shows their projected distance in arcsec and kpc. Bottom row: Each object's continuum map is overlaid with the identical CO J = 2–1 M0 map. The noise level is assessed directly from the continuum map and is similarly marked at the bottom of each panel.

same settings but with the `cube` specmode, to produce cubic data at 10 km s^{-1} per channel. Spectra from this TCLEAN cubic data are extracted to refine the line fitting, leading to a repeated TCLEAN run with the updated line frequency centre and FWHM.

From the newly acquired cubic data, we individually derive the spectrum for each source, with the apertures identified as white ellipses in the panels (d) of Figs 4–8. Subsequently, we perform measurements of the full width at half maximum (referred to as W_{50}) for the CO J = 2−1 line in accordance with Tiley et al. (2016). In their research, various fitting functions were rigorously evaluated to assess their accuracy in replicating the line width of simulated galaxy spectra across a wide range of parameters, including amplitude-to-noise ratio (A/N), inclination, and rotation velocity. Their results reveal that a parabolic function flanked by two mirrored half-Gaussians, termed a 'symmetric Gaussian Double Peak function,' displayed the least bias across much of the parameter space. This function is represented as:

$$f(v) = \begin{cases} A_{\rm G} \times {\rm e}^{\frac{-[x-(c-w)]^2}{2\sigma^2}} & x < c-w, \\ A_{\rm C} + a\,(x-c)^2 & c-w \le x \le c+w, \\ A_{\rm G} \times {\rm e}^{\frac{-[x-(c+w)]^2}{2\sigma^2}} & x > c+w \end{cases} \quad (2)$$

where x denotes the observed frequency, c is the line centre, $w > 0$ represents the half-width of the parabola, $\sigma > 0$ stands for the width of the two half-Gaussians centred at $c \pm w$, both sharing the same peak flux $A_G > 0$. Additionally, we impose the condition $A_{\rm C} \le 0.8A_{\rm G}$ to ensure fitting stability.

Yet, not all galaxies inherently show double-peaked line profiles. This feature is influenced by aspects such as inclination and gas distribution (e.g. Lavezzi & Dickey 1997; Davis et al. 2011). Therefore, we initially applied both a double-peaked Gaussian model and a typical single Gaussian model to fit the CO J = 2-1 lines extracted from our sources. The fitting was performed using the Python package `lmfit`, using the Levenberg–Marquardt (leastsq) algorithm for optimization. To evaluate the fitting quality, we refer to three criteria: the Akaike information criterion (AIC; Akaike 1998), Bayesian information criterion (BIC; Schwarz 1978), and reduced chi-square assessment between the models. The model with lower values in at least two of these criteria was considered preferred. Panels (g) and (h) in Figs 4–8 depict the chosen model and its 3σ uncertainty as a red curve with shaded regions.

Using the proposed model, we calculate the W_{50} values for the CO spectral lines in the following manner. For a double-peaked Gaussian fit:,

$$W_{50} = 2(w + \sqrt{2\ln 2}\sigma) \quad (3)$$

and for a single Gaussian fit:,

$$W_{50} = 2\sqrt{2\ln 2}\sigma \quad (4)$$

Initially, we execute these fittings in the frequency domain to ascertain the precise position of the CO line. Subsequently, we translate the width W_{50} into velocity, as listed in column (5) of Table 3.

Next, we construct the moment 0 (M0) map utilizing the W_{50} values. For each source, we determine the frequency span within $1.5\times W_{50}$, which is the central frequency $\pm\, 0.75\times W_{50}$ [indicated by the blue vertical dashed lines in Figs 4–8 (g) and (h) panels with precise frequencies provided in the respective sections]. Channels within this frequency span are utilized to create the M0 map through the `immoments` function. In scenarios where detections occur for both sources, we select the minimum channels that encompass $1.5\times W_{50}$ of both entities. The M0 outcomes are depicted as contours in Fig. 3 and also within panel (a) of Figs 4–8. The background noise level ($\sigma_{\rm bkg}$) is calculated from the standard deviation in the residual map and is annotated at the panels' lower sections. Contour levels commence at $3\sigma_{\rm bkg}$ and progress in increments of $3\sigma_{\rm bkg}$. Even though generally negligible, negative $3\sigma_{\rm bkg}$ signals are represented as white dashed contours.

On the M0 map, we execute the 2D Gaussian fitting process using both the `imfit` tool in CASA and the interactive tool in CARTA. The findings exhibit a consistency with a variation of approximately 10 per cent in both integrated and peak flux measurements. The

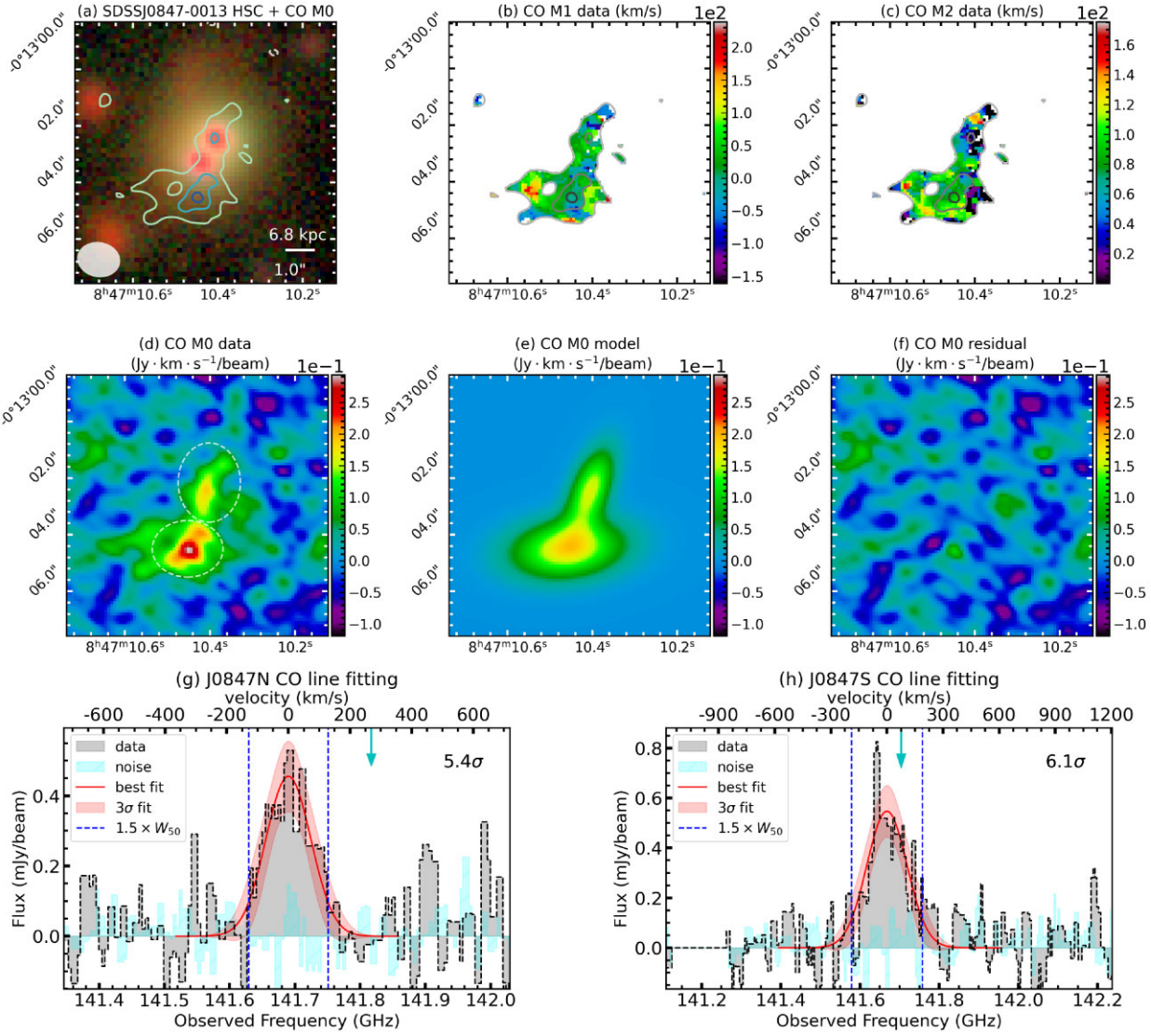

Figure 4. CO J = 2–1 properties of SDSS J084710.40−001302.6. (a) CO M0 (intensity) map as described in Section 2.3. The underlying image is generated from Subaru/HSC *g*-, *r*-, and *i*-band data. The ellipse at the bottom left indicates the beam size of our ALMA observation, and the projected optical separation between the two nuclei is shown as the scale bar at the bottom right with angular and physical scales. (b) CO M1 (velocity) map generated with `immoment` in unit of km s^{-1}. The velocity centre is selected to be the centre of the Gaussian model of the CO profile in panel (g). (c) CO M2 (dispersion) map generated with `immoment` in unit of km s^{-1}. (d) Same CO M0 map as in panel (a) with the flux level shown by the scale bar. (e) 2D gaussian model of CO M0 map generated from `imfit`. (f) CO residuals of the M0 map after subtracting the model in panel (e) from the data in Panel (d). (g) and (h) Emission line profiles of the two sources extracted from the regions marked in panel (d) together with the noise spectra extracted from offset regions from the sources, the best-fitting model with 3σ uncertainties from LMFIT, and W_{50} of the emission line. The arrows at the top indicate the expected position of the CO line based on the optical spectroscopic redshift. The signal-to-noise ratio of the line is noted at the top right, as defined in Section 2.3.2.

most suitable models derived from `imfit` are illustrated in panels (e) of Figs 4 through 8, while the corresponding residual maps are displayed in panels (f). In column (7) of Table 3, we provide the integrated flux $S_{\mathrm{CO(2\text{-}1)}}\delta v$ as measured by `imfit`. This integrated flux is subsequently employed to compute the line luminosity following the method of Solomon, Downes & Radford (1992):

$$L'_{\mathrm{line}} = 3.25 \times 10^7 \times S_{\mathrm{line}}\,\delta v \frac{D_L^2}{(1+z)^3 \nu_{\mathrm{obs}}^2}\ \mathrm{K\ km\ s^{-1} pc^2} \quad (5)$$

where $S_{\mathrm{line}}\delta v$ refers to the integrated CO J = 2–1 flux as outlined earlier. In this context, D_L represents the luminosity distance in Mpc, while ν_{obs}^2 denotes the observed frequency of the emission line. Results are expressed as log $L'_{\mathrm{CO(2\text{-}1)}}$ in column (8) of Table 3. Additionally, `imfit` provides the peak flux of the optimal model ($S^{\mathrm{peak}}_{\mathrm{CO(2\text{-}1)}}$), which we utilize to calculate the signal-to-noise ratio (S/N) of the emission line. Thus, S/N $= S^{\mathrm{peak}}_{\mathrm{CO(2\text{-}1)}}/\sigma_{\mathrm{bkg}}$, as indicated on the upper right of panels (g) and (h) in Figs 4–8.

Sizes of the sources in interferometric data are typically measured in the *uv*-plane to benefit from uncorrelated noise and avoid imaging artifacts like deconvolution errors (e.g. Fujimoto et al. 2020; Pozzi et al. 2024; Tan et al. 2024). However, according to Tan et al. (2024), performing *uv*-plane profile fitting requires an S/N of at least 50 to yield meaningful and consistent results. The highest S/N of our sources is around 13σ, which proved inadequate for the `uvmodelfit` procedure, as it struggles to converge with either Gaussian or Disc models. Consequently, we rely on the `imfit`

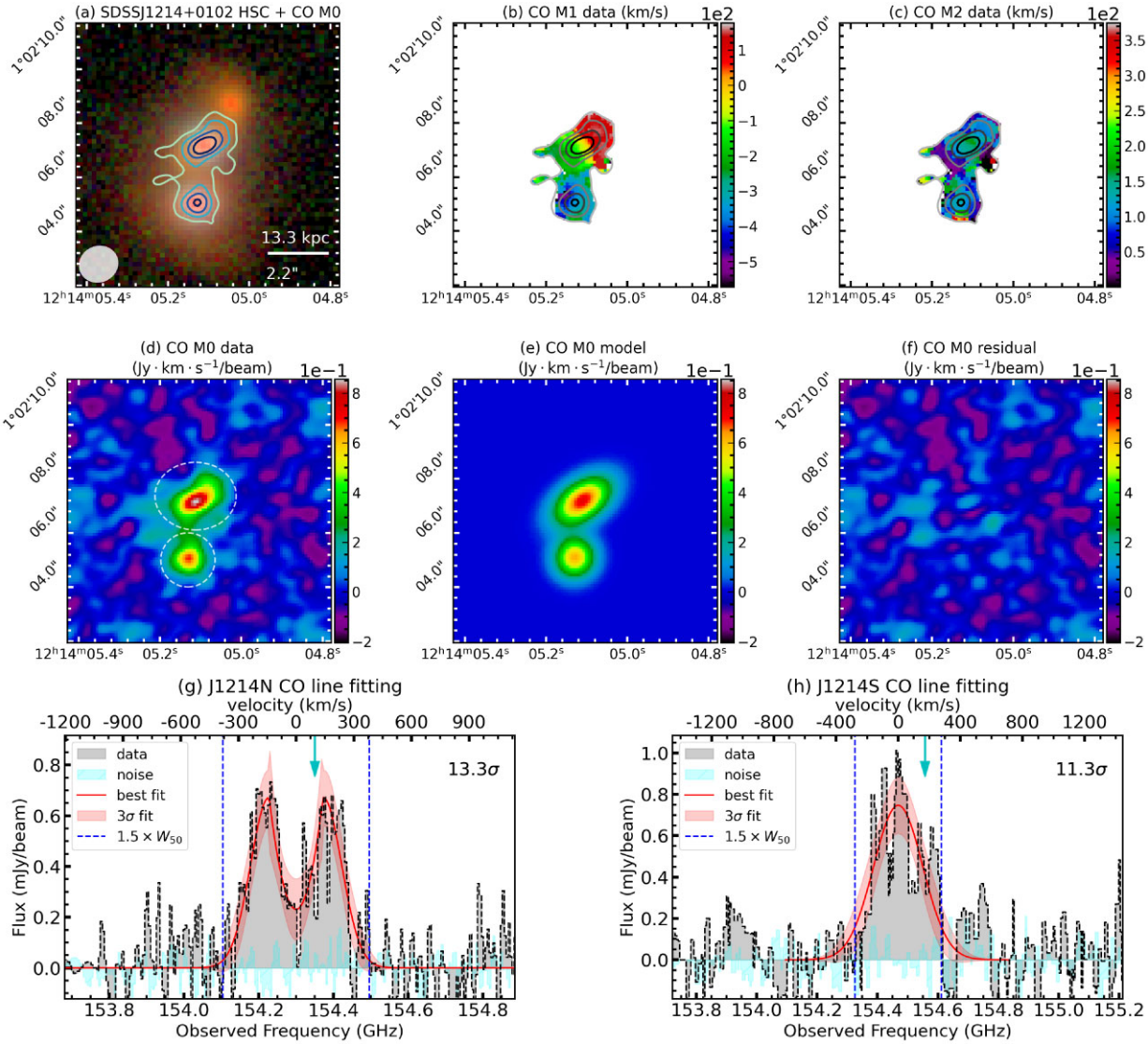

Figure 5. CO properties of SDSS J121405.12+010205.1. The format is similar to Fig. 4.

results on the image plane, which are reported in Table 3, column (6). The sizes, given as the FWHM for the major and minor axes, are presented after deconvolution. We further compared these measured sizes with the beam sizes listed in Table 2. When a source's size is less than 1.5 times the beam area, it is considered unresolved.

Subsequently, we generate the velocity moment 1 (M1) and dispersion moment 2 (M2) maps using `immoments` over the same frequency span as the M0 maps, only retaining pixels above the $3\sigma_{\rm bkg}$ threshold. These are illustrated in Fig. 4–8 panels (b) and (c), with M0 contours overlaid.

2.3.3 *Molecular gas masses and fractions*

To determine the molecular gas mass and fraction for our dual quasars, we initially convert $L'_{\rm CO(2\text{-}1)}$ into CO J = 1–0 luminosity ($L'_{\rm CO(1\text{-}0)}$) using an excitation correction factor $R_{21} = L'_{\rm CO(2\text{-}1)}/L'_{\rm CO(1\text{-}0)} = 0.62$, derived from the average findings of low-z PG quasars (Shangguan et al. 2020). For all of their sources with detections of $L'_{\rm CO(2\text{-}1)}$ and $L'_{\rm CO(1\text{-}0)}$, the values of R_{21} range from a maximum of 0.90 to a minimum of 0.49 [see also Carilli & Walter (2013) suggesting $R_{21} = 0.99$]. The $L'_{\rm CO(1\text{-}0)}$ is empirically linked to the gas H_2 by a conversion factor $\alpha_{\rm CO}$, measured in units of $M_\odot(K \cdot km \cdot s^{-1} \cdot pc^2)^{-1}$. It is important to note that $\alpha_{\rm CO}$ varies depending on the density, temperature and metallicity of the gas (refer to Bolatto, Wolfire & Leroy 2013, for a detailed review). The literature cites various values for $\alpha_{\rm CO}$, generally ranging between $\alpha_{\rm CO} = 0.8$–4.3 (e.g. Downes & Solomon 1998; Bolatto et al. 2013). In our case, we select $\alpha_{\rm CO} = 3.1$, based on Shangguan et al. (2020). With the selected R_{21} and $\alpha_{\rm CO}$, we determined the molecular gas mass $M_{\rm molgas} = \alpha_{\rm CO} \times L'_{\rm CO(2\text{-}1)}/R_{21}$, as shown in Table 3 column (9). We then calculated the ratio of the molecular gas mass to the stellar mass $\mu_{\rm molgas} = M_{\rm molgas}/M_*$ in column (10). Details regarding the measurement of stellar mass M_* are provided in Section 2.2.

3 RESULTS

3.1 CO detection

In the top row of Fig. 3, we present the *gri* colour images of the five dual quasars, taken from the HSC, with the ALMA CO J = 2–1

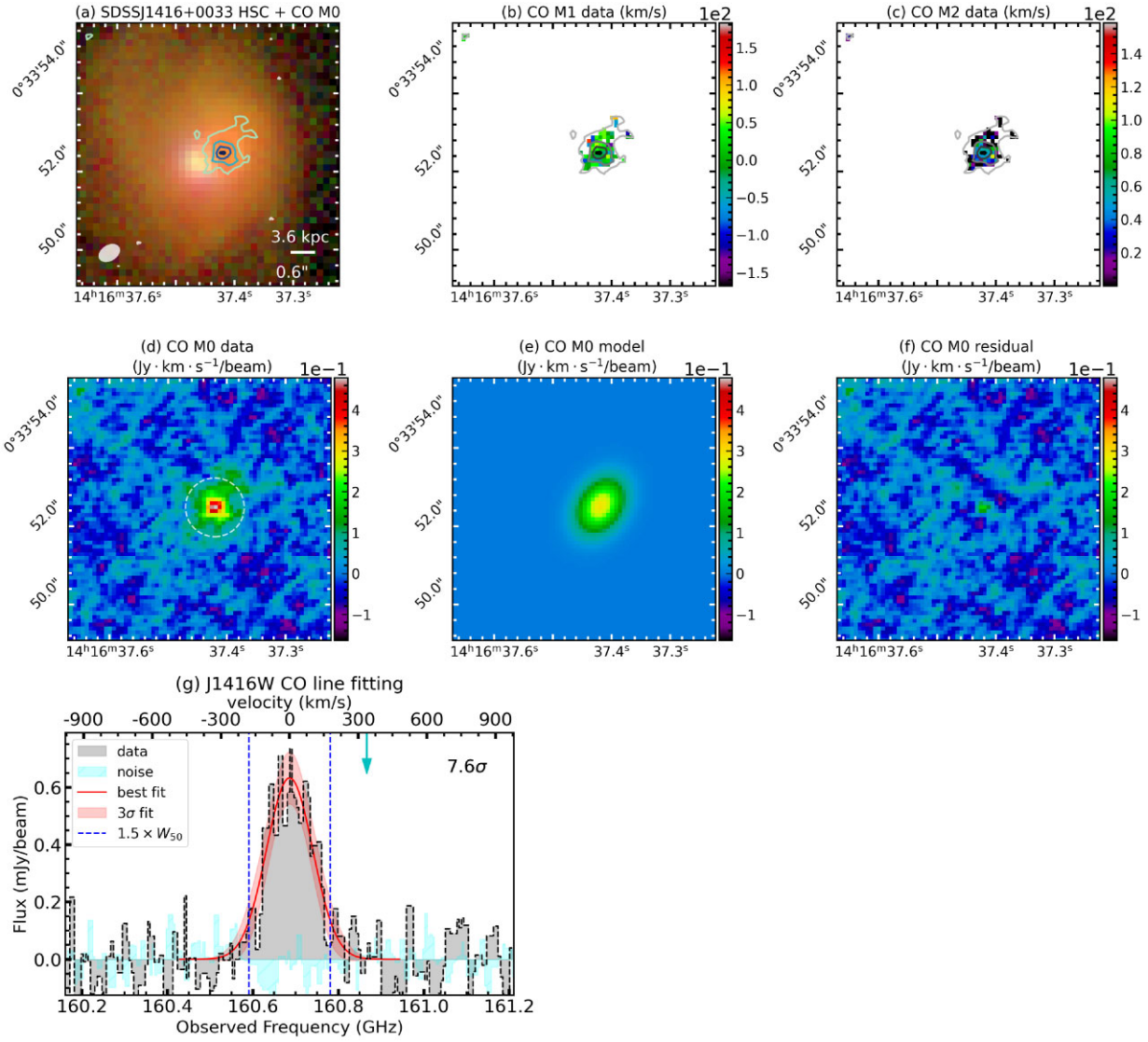

Figure 6. CO properties of SDSS J141637.44+003352.2. The format is similar to Fig. 4.

contours superimposed. These contours are plotted at intervals $3\sigma_{\rm bkg}$, beginning at the same level. The value of $\sigma_{\rm bkg}$ is determined from the residual map after removing the optimal `imfit` model from the data. The optical centres of the point sources are indicated by white crosses derived from the HSC *i*-band image, and their projected separations are indicated in the bottom right. Using our S/N definition based on the peak of the optimal `imfit` model (Section 2.3), we confirm that the line CO J = 2–1 line is detected at 5σ or stronger in eight out of ten quasars. It is noted that the CO centre of J0847S is offset by approximately 1.2 arcsec (8.2 kpc) from the optical centre; in contrast, the CO emissions of the remaining seven detections align with the optical quasar positions. The FWHM dimensions, major and minor, are detailed in Table 3 (column 6). Although `imfit` gives sizes for all sources, most are nearly unresolved due to beam size constraints (see Table 2 column 6). Exceptions include J0847S, resolved into 6.5 ± 1.5 beam sizes, and J1416W, resolved into 12.9 ± 1.9 beam sizes, while the other six are $\lesssim$2 beam sizes. For the non-detected sources, we estimate a size of 1 beam, with $S_{\rm CO(2\text{-}1)}$ upper limits set to $3\sigma_{\rm bkg}$ within one beam (refer to Table 3 column 7). Furthermore, using the extracted 1D spectral profile (detailed for each pair in Section 3.2), we determine the frequency centre and FWHM (W_{50}) of the CO line (Table 3 columns 4 and 5).

3.2 Details of individual pairs

In this section, we explore the details of each pair of quasars, presenting our findings in a dedicated figure for each source. Taking Fig. 4 as our template, we maintain a uniform format:

(i) Subaru/HSC colour image with CO J = 2–1 M0 map superimposed as contours (panel a).

(ii) Velocity (M1; panel b) and dispersion (M2; panel c) maps calculated with `immoment` in km s^{-1}.

(iii) CO M0 image displaying flux levels (panel d).

(iv) Optimal fit of the model (via `imfit`) based on the M0 data (panel e).

(v) The residual map generated by subtracting the model from the data (panel f).

(vi) 1D spectra for both sources (panels g and h) extracted from the white dashed elliptical regions (apertures) in panel (d), shown as

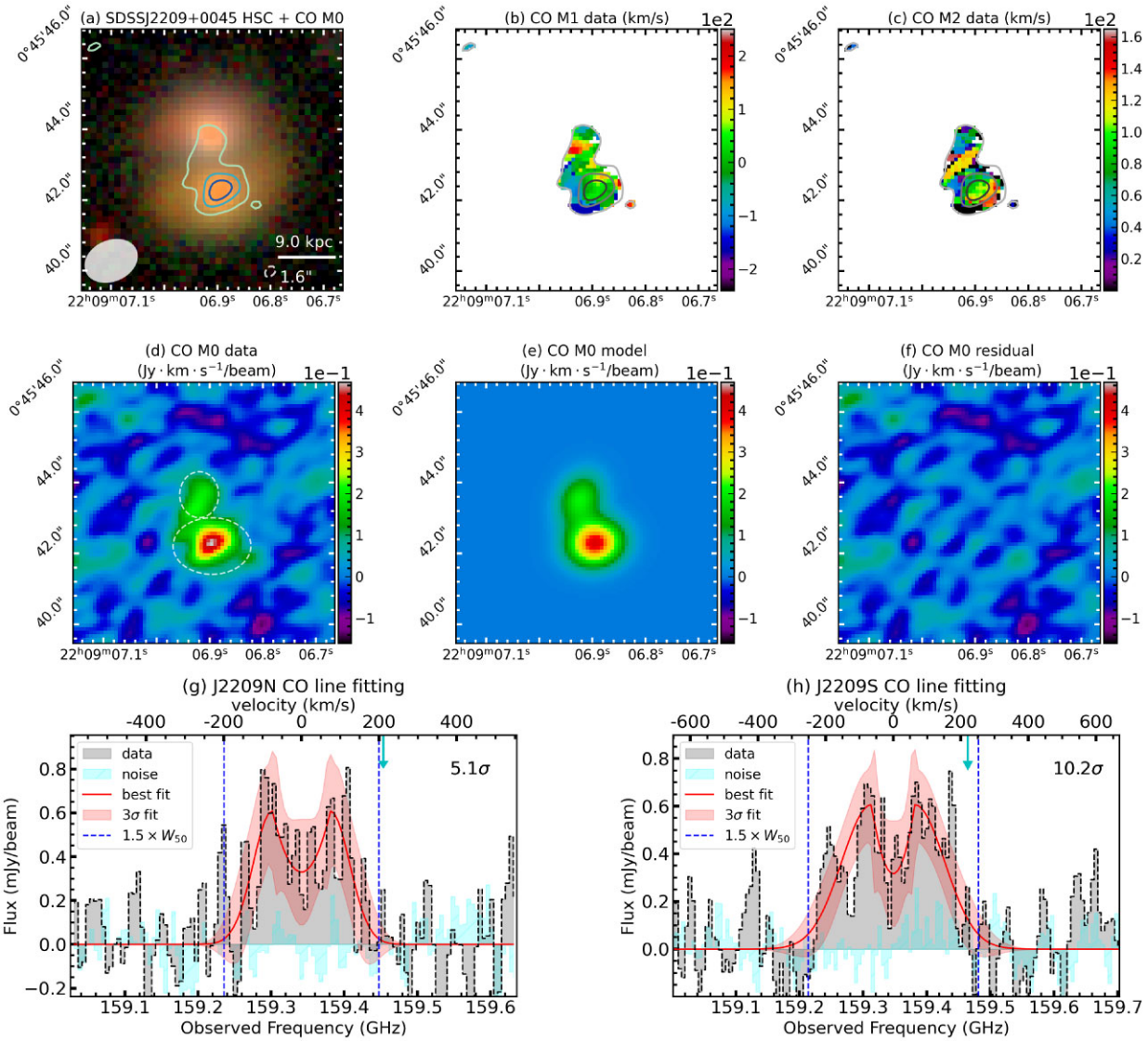

Figure 7. CO properties for SDSS J220906.91+004543.9. The format is similar to Fig. 4.

grey histograms. The noise spectrum appears in cyan. The optimal fit and the 3σ confidence interval are indicated by the red curve with shadows. The W_{50} of the emission line is denoted by vertical blue dashed lines. The anticipated frequency of the CO J = 2–1 line based on the optical spectroscopic redshift is marked by a cyan arrow above the 1D spectra. The S/N of the emission line (see definition in Section 2.3.2) is mentioned at the top right.

3.2.1 SDSS J084710.40−001302.6

This system, initially identified by Inada et al. (2008) while investigating lensed quasars using the Keck/LRIS, consists of two point sources located 1.0 arcsec apart at redshift $z = 0.626$ ($R_\perp = 6.8$ kpc). In our reanalysis of the Keck/LRIS 1D spectrum using PSYQSOFIT, we found a 6.9σ detection of the broad Mg II line with $W_{50} = 6945\,\mathrm{km\,s^{-1}}$ for J0847N, and an 8.4σ detection with $W_{50} = 7911\,\mathrm{km\,s^{-1}}$ for J0847S. However, the Hβ lines in both sources are notably weak and only allow fitting with a narrow component. The spectrum of J0847N is bluer than that of J0847S, with the ratio dropping from 3 at approximately 3500 Å to 1 at 8000 Å. The O [III]/H β ratio stands at 10.5 for J0847N and 15.7 for J0847S. These observations lead us to further support that this is a quasar pair, not a lensed quasar. According to the Mg II virial method, the M_{BH} ratio of J0847N to J0847S is 1.4:1. Positioned between the two sources, the host galaxy features an effective radius of $R_e = 0.94''$ (4.5 kpc) in HSC i-band and stellar mass $M_* = 10^{10.95}\,\mathrm{M_\odot}$.

Panels (a), (b), and (c) of Fig. 4 present its M0, M1, and M2 maps generated in the 141.629 to 141.751 GHz range. The double-component `imfit` model (panel e) evaluates a line peak signal-to-noise ratio of 5.4σ for J0847N and 6.1σ for J0847S. Single Gaussian profiles adequately fit both spectral line shapes (panels g and h), with widths W_{50} of $172 \pm 14\,\mathrm{km\,s^{-1}}$ for J0847N and $252 \pm 18\,\mathrm{km\,s^{-1}}$ for J0847S, respectively. J0847N's deconvolved CO emitting region spans 2.0 ± 1.4 beam area, equating to FWHM dimensions of 16 kpc $\times$ 4 kpc. In contrast, J0847S is larger, covering 6.5 ± 1.5 beam area, which corresponds to 21 kpc $\times$ 10 kpc.

A notable feature in this system is the CO centre of J0847S being offset from its optical centre by an angular separation of 1.2 arcsec and a projected physical distance of 8.2 kpc. No optical counterpart is visible for this offset gas blob in the HSC image, at a depth

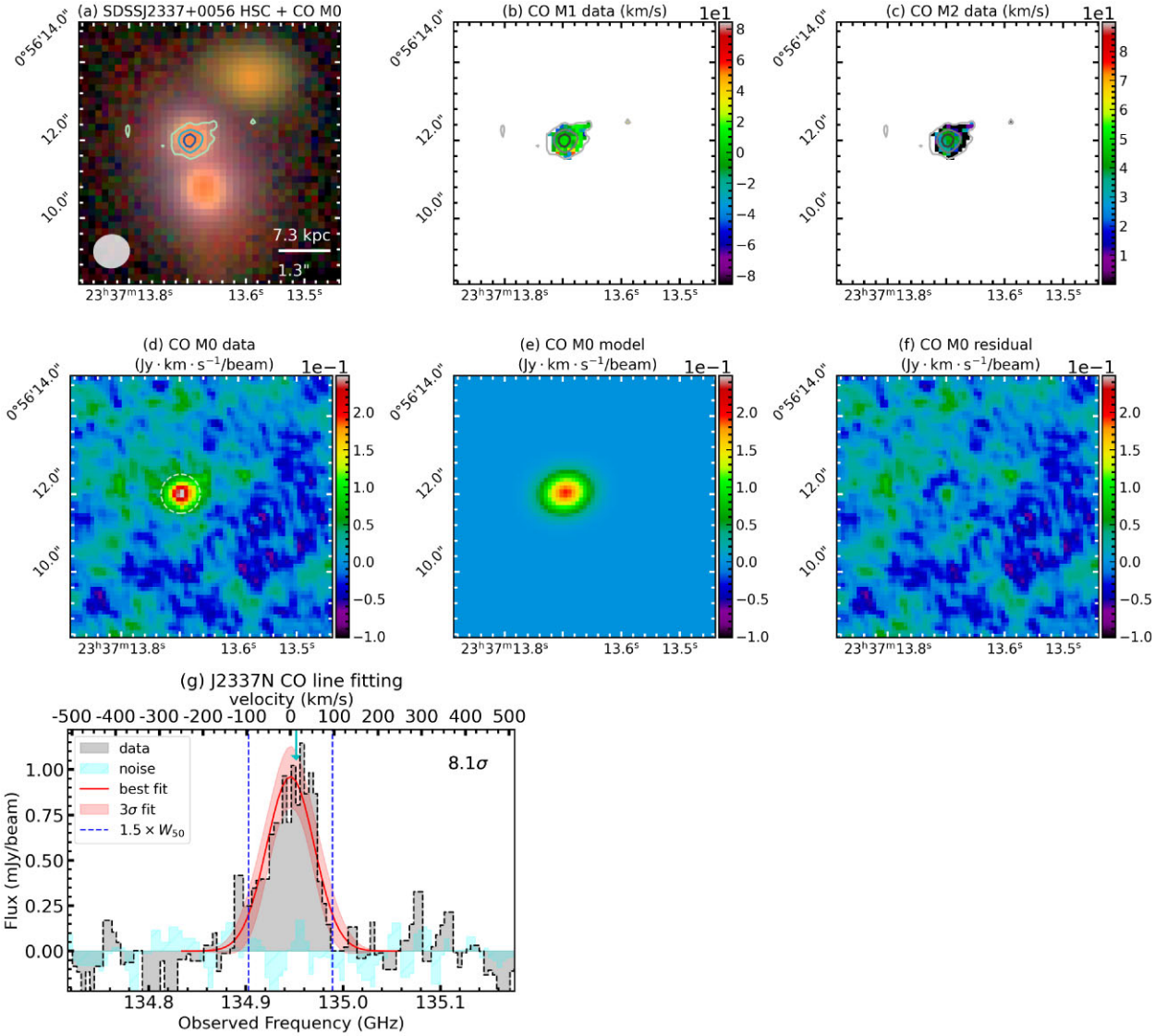

Figure 8. CO properties for SDSS J233713.66+005610.8. The format is similar to Fig. 4.

of 5σ reaching approximately 26.5 mag, and its position was also not captured by the LRIS slit (Silverman et al. 2020). The optical emission lines for J0847N and J0847S differ by 240 km s^{-1}, whereas the CO centres are approximately 42 km s^{-1} apart. The difference between the CO and optical redshifts is 277 km s^{-1} for J0847N and 55 km s^{-1} for J0847S, as indicated by the cyan arrows in panels (g) and (h) of Fig. 4. Maps M1 and M2 for both sources are largely unresolved. Our hypothesis is that this detached gas blob is the result of ram pressure stripping (Kapferer et al. 2008) or may have been expelled due to AGN feedback and/or interactions involving multiple bodies (Carniani et al. 2017).

3.2.2 SDSS J121405.12+010205.1

The system was verified by Silverman et al. (2020) as consisting of dual quasars at a redshift of $z = 0.493$, with a separation of 2.2 arcsec ($R_\perp = 13.3$ kpc) between them. We conducted a reanalysis of the reduced 1D spectra obtained from Keck/LRIS using PYQSOFIT. The broad Mg II line for J1214N is measured with a 14.5σ significance and an FWHM of 9057 km s^{-1}, whereas for J1214S, it is detected with a 14.6σ significance and W_{50} of 4984 km s^{-1}. For the broad Hβ components, J1214N presents a 10.0σ significance with W_{50} = 11 039 km s^{-1}, and J1214S shows a 6.0σ significance with W_{50} = 7838 km s^{-1}. The O [III]/H β ratio is 3.9 for J1214N and 3.5 for J1214S. J1214S has a slightly steeper continuum slope compared to J1214N. These spectral differences imply that they form a physical pair of quasars. A third red source in the northwest is outside the slit coverage and is undetected by ALMA. The alignment of these three systems differs from that of HSC lenses (e.g. Chan et al. 2020). The Mg II virial method reveals that the black hole mass ($M_{\rm BH}$) ratio between J1214N and J1214S is 3.8:1, whereas their stellar mass (M_*) ratio is 1:6.

The CO maps shown in Fig. 5 are produced at frequencies ranging from 154.104 to 154.612 GHz. According to the model, the line shows a peak signal-to-noise ratio of 13.2σ for J1214N and 11.3σ for J1214S. The line profile for J1214N is best described by a double-peaked Gaussian with $W_{50} = 508 \pm 29$ km s^{-1}, while the profile of J1214S resembles a single Gaussian with $W_{50} = 340 \pm 60$ km s^{-1}. The CO and optical centres are separated by 120 km s^{-1} in J1214N and 180 km s^{-1} in J1214S. Furthermore, the centre of the CO line

Table 3. Detailed properties of CO J = 2-1 for the analysed dual quasars as processed using CASA are summarized here. Refer to Section 2 for a comprehensive explanation of the methodology. Column (1): Abbreviated names of sources, based on their relative positions in each quasar pair. Columns (2)–(3): Source positions determined via `imfit` on the average CO line map. Columns (4)–(5): Central frequency and W_{50} of the CO J = 2–1 line profile. Column (6): Object sizes noted as major and minor axis FWHM, corrected for beam deconvolution. Column (7): Integrated CO flux extracted from the M0 map, using `imfit`. For sources not detected, we considered a size equivalent to 1 beam, with upper limits set at $3\sigma_{\rm bkg}$. Column (8): CO J = 2–1 luminosity derived from equation (5). Column (9): Molecular gas mass computed with $R_{21} = 0.62$ and $\alpha_{\rm CO} = 3.1$ (Shangguan et al. 2020). Column (10): Ratio of molecular gas mass to stellar mass ($\mu_{\rm molgas} = M_{\rm molgas}/M_*$).

Name	RA	Dec.	Freq.	W_{50}	Size	$S_{\rm CO(2-1)}\delta v$	log $L'_{\rm CO(2-1)}$	log $M_{\rm molgas}$	$\mu_{\rm molgas}$
	(hh:mm:ss)	(dd.mm.ss)	(GHz)	(km s^{-1})	(arcsec)	(Jy km s^{-1})	(K km s^{-1} pc^2)	($M_\odot$)	(ratio)
(1)	(2)	(3)	(4)	(5)	(6)	(7)	(8)	(9)	(10)
J0847N	08:47:10.41	−00:13:02.42	141.69	172 ± 14	2.30 ± 0.54; 0.59 ± 0.39	0.61 ± 0.13	9.50 ± 0.09	10.20 ± 0.09	17.8 ± 3.8 per cent
J0847S	08:47:10.45	−00:13:04.51	141.67	252 ± 18	3.07 ± 0.49; 1.44 ± 0.24	1.4 ± 0.21	9.86 ± 0.07	10.56 ± 0.07	41.0 ± 6.1 per cent
J1214N	12:14:05.11	01:02:07.24	154.30	508 ± 29	1.70 ± 0.19; 0.79 ± 0.12	2.27 ± 0.22	9.86 ± 0.04	10.56 ± 0.04	301.4 ± 29.2 per cent
J1214S	12:14:05.13	01:02:05.08	154.47	340 ± 60	unresolved	1.28 ± 0.17	9.61 ± 0.06	10.31 ± 0.06	28.7 ± 3.8 per cent
J1416W	14:16:37.42	00:33:52.48	160.69	273 ± 13	1.19 ± 0.12; 0.86 ± 0.09	4.03 ± 0.38	9.99 ± 0.04	10.69 ± 0.04	31.9 ± 3.0 per cent
J1416E	–	–	–	–	–	< 0.11	< 8.43	< 9.13	< 0.9 per cent
J2209N	22:09:06.92	00:45:43.47	159.34	270 ± 40	unresolved	0.39 ± 0.12	9.00 ± 0.13	9.70 ± 0.13	26.5 ± 8.2 per cent
J2209S	22:09:06.90	00:45:42.26	159.35	340 ± 40	unresolved	0.85 ± 0.13	9.34 ± 0.07	10.04 ± 0.07	26.4 ± 4.0 per cent
J2337N	23:37:13.70	00:56:12.00	134.95	128 ± 8	0.87 ± 0.17; 0.60 ± 0.14	0.57 ± 0.09	9.58 ± 0.07	10.28 ± 0.07	47.9 ± 7.6 per cent
J2337S	–	–	–	–	–	< 0.07	< 8.67	< 9.37	< 1.1 per cent

for J1214S is blueshifted by 330 km s^{-1} relative to J1214N. The deconvolved CO emitting region for J1214N spans 1.9 ± 0.4 beam area, equivalent to 10.3 kpc × 4.8 kpc in FWHM, while for J1214S, it covers 1.1 ± 0.3 beam area and is considered unresolved.

J1214N is the only source in this work that shows a clear velocity gradient in its M1 map, as shown in panel (b) of Fig. 5. This feature is resolved at approximately two beam sizes. The velocity reference point is established at the centre of J1214N's line profile at 154.30 GHz. The components that are blue-shifted and red-shifted show a spatial separation of about one beam size in both the cube data and the integrated M1 map. The v/σ ratio for J1214N ranges from 0.5 to 2. This structure suggests the presence of either a merger front or a rotation disc in J1214N, further explored in Section 4.2. Furthermore, J1214N has the highest $\mu_{\rm molgas}$ among our sources, with a value around 300 per cent.

3.2.3 SDSS J141637.44+003352.2

This system was identified by Silverman et al. (2020) as a dual quasar at z = 0.434 with 0.65″ ($R_\perp = 3.9$ kpc) separation between the two nuclei. Their Keck/LRIS spectrum was blended, and the 1D spectrum was extracted from the extended wings of the 2D profile. Subsequent Gemini/NIFS z-band IFU observation resolved the two nuclei, and the 1D spectrum was extracted from two circular apertures centred on each source. We combined the two parts of the spectrum by matching the z-band flux of the Keck/LRIS spectrum to that of Gemini/NIFS, and reanalysed it with PYQSOFIT. Consequently, J1416E [left blue source in panel (a) of Fig. 6] reveals a 6.9σ detection of Mg II with $W_{50} = 6618$ km s^{-1}, and a 11.6σ detection of H α with $W_{50} = 3245$ km s^{-1}. J1416W (the right red source) reveals a 3.8σ detection of Mg II with $W_{50} = 11\,857$ km s^{-1}, 5.7σ detection of H β with $W_{50} = 14\,160$ km s^{-1}, and 2.9σ detection of H α with $W_{50} = 6294$ km s^{-1}. The broad emission lines are overall weak in J1416W, while the existence of high-ionization narrow lines like [O III] and [Ne V] in its spectrum suggested quasar-origin emission. Together with its red colour in the HSC image, Silverman et al. (2020) classified J1416W as a type-1.5 quasar with some level of obscuration. Based on the H α virial method, the $M_{\rm BH}$ ratio between J1416W and J1416E is 3.5:1. The decomposed HSC image suggests that the pair shares a single host galaxy with $R_e = 1.56''$ (9.4 kpc) and $M_* = 10^{11.19}$M$_\odot$.

The CO maps in Fig. 6 are generated between 160.591 and 160.781 GHz. CO emission is associated with the type-1.5 companion J1416W, with a 3σ upper limit of 0.11 Jy km s^{-1} for J1416E. Based on a single-component model, the peak signal-to-noise ratio of the line is 7.8σ. Its profile is fitted with a single Gaussian with $W_{50} = 237 \pm 13$ km s^{-1}. Its centre is offset from the optical emission lines by 335 km s^{-1}. The deconvolved CO emitting area corresponds to 12.9 ± 1.9 beam area, with a physical size of 7.2 kpc × 4.8 kpc. The $\mu_{\rm molgas}$ of J1416W is ∼30 per cent, while that of J1416E is $\lesssim$1.0 per cent.

3.2.4 SDSS J220906.91+004543.9

This system, reported by Tang et al. (2021), is classified as a dual quasar at $z = 0.446$, exhibiting a separation of 1.63″ ($R_\perp = 9.2$ kpc). We conducted a reanalysis of the Subaru/FOCAS spectra using PYQSOFIT, which identified a 9.5σ detection of the broad H β line with $W_{50} = 5064$ km s^{-1} and a 10.1σ detection of the broad H α line with $W_{50} = 3398$ km s^{-1} for J2209N. For J2209S, the broad H β line was detected with 5.7σ significance at $W_{50} = 4255$ km s^{-1},

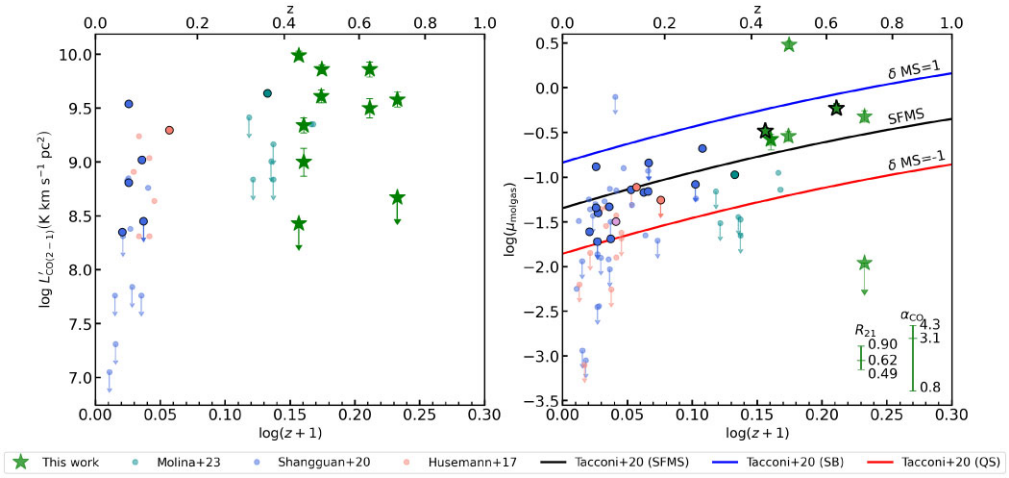

Figure 9. CO luminosity ($L'_{CO(2-1)}$, left panel) and molecular gas to stellar mass ratio ($\mu_{molgas} = M_{molgas}/M_*$, right panel) of our dual quasars (stars marks) in comparison with single quasars from previous studies (dots). The larger dots with outlines represent single quasars identified as mergers. In the right panel, we also show the best-fitting results from Tacconi, Genzel & Sternberg (2020) for starburst (SB), star-forming main sequence (SFMS), and quiescent (QS) galaxies, depicted as the solid curves from top to bottom, respectively. The error bars for R_{21} and α_{CO} are indicated in the bottom right corner. The pair J0847 and J1416 are condensed into a single data point (stars with outlines), since there is only a single M_* measurement for each pair.

while the broad Hα was detected with a 6.3σ significance at $W_{50} = 2827\,\mathrm{km\,s^{-1}}$. J2209N exhibits a bluer continuum compared to J2209S, with the spectral ratio decreasing from approximately 2 at 6000 Å to approximately 1 at 10 000 Å. The O [III]/Hβ ratio is 6.3 for J2209N and 2.2 for J2209S. Consequently, this system is determined to be a physical pair rather than a lensed quasar. According to the Hβ virial method, the M_{BH} ratio between J2209N and J2209S is 2:1, whereas the M_* ratio is 1:2.

The CO observations illustrated in Fig. 7 span frequencies between 159.236 and 159.447 GHz. Using the dual component model, the maximum signal-to-noise ratio of the line is determined to be 5.1σ for J2209N and 10.2σ for J2209S. These profiles are modelled with double-peaked Gaussians, indicating $W_{50} = 270 \pm 40\,\mathrm{km\,s^{-1}}$ for J2209N and $W_{50} = 340 \pm 40\,\mathrm{km\,s^{-1}}$ for J2209S. Both CO centres are approximately 200 km s^{-1} redshifted relative to their optical lines. The deconvolved CO emission region for J2209N spans 0.8 ± 0.7 beam area, and for J2209S, it spans 1.1 ± 0.5 beam area, suggesting that they are unresolved.

3.2.5 SDSS J233713.66+005610.8

The system, as identified by Tang et al. (2021), is a dual quasar discovered at z = 0.708 with a 1.34 arcsec separation (corresponding to $R_\perp = 7.6$ kpc). Upon reanalysing the Gemini/GMOS spectra using PYQSOFIT, we identified a 7.0σ detection of broad Hβ at $W_{50} = 3463$ km s^{-1}, and a 4.1σ detection of broad Hγ at $W_{50} = 3490\,\mathrm{km\,s^{-1}}$ for J2337N. For J2337S, the broad Hβ is detected with a significance of 13.5σ and $W_{50} = 4237\,\mathrm{km\,s^{-1}}$, while the broad H$\gamma$ shows a detection of 4.7σ and $W_{50} = 4438\,\mathrm{km\,s^{-1}}$. Broad and blueshifted [O III] components are observed in both quasars, with $W_{50} = 408\,\mathrm{km\,s^{-1}}$ for J2337N and 696 km s^{-1} for J2337S. The two sources exhibit nearly the same continuum slopes, but J2337S generally displays broader line widths compared to J2337N. Therefore, we affirm this system as a physically paired quasar system. The Hβ virial method estimates a M_{BH} ratio of 1:2.1 between J2337N and J2337S, and a M_* ratio of 1:5.5.

The CO data depicted in Fig. 8 span frequencies between 134.903 and 134.989 GHz. According to a single-component model analysis, the CO J = 2–1 line was detected with a significance level of 8.1σ only for J2337N. The 3σ upper threshold for the same M0 map measures 0.07 Jy km s^{-1}. The profile of this line is accurately modelled by a single Gaussian with $W_{50} = 128 \pm 8\,\mathrm{km\,s^{-1}}$. The centre of the CO emission is nearly aligned with that of the optical emission lines in terms of redshift. The deconvolved region of CO emission extends over 1.9 ± 0.6 beam area, corresponding to a physical size of 6.2 kpc × 4.3 kpc. The μ_{molgas} for J2337N is approximated to be about 48 per cent, while for J2337S it is not more than 1 per cent.

4 DISCUSSION

Our findings indicate that dual quasars generally have significant molecular gas supplies, with M_{molgas} ranging from $10^{9.6-10.5}$ M$_\odot$ and μ_{molgas} spanning 18–50 per cent with an exception of 301 per cent. In this section, we begin with a statistical evaluation to qualitatively assess if these systems are quenched. We then investigate the diverse distribution of molecular gas across our dual quasars. This analysis seeks to provide insights into quasar behavior during galaxy mergers and relate these observations to the larger context of black hole-host coevolution.

4.1 Do dual quasars show signs of gas depletion?

Our objective is to ascertain if dual quasars exhibit signs of gas depletion that could suggest the quenching of future star formation. To explore this issue, we initially examine the CO J = 2–1 luminosity ($L'_{CO(2-1)}$) and the ratio of molecular gas to stellar mass (μ_{molgas}) characteristics of our dual quasars, as detailed in Table 3.

In Fig. 9, the left panel displays $L'_{CO(2-1)}$ as a function of redshift. The green stars denote our dual quasars, while the colored dots represent the comparative single quasars. The PG quasars from Molina et al. (2023) serve as a reasonable comparison to our dual quasars with respect to redshift and black hole characteristics, such as L_{bol} and M_{BH}. We utilized the `logrank test` (Mantel–Cox test, Mantel et al. 1966), facilitated by the LIFELINES PYTHON package, to evaluate the differences in $L'_{CO(2-1)}$ values between their samples

and our dual quasars. Including the upper limits in our analysis, the test produced a p-value of 0.14, suggesting that there is no significant discrepancy in $L'_{\rm CO(2\text{-}1)}$ between the two data sets. Other single quasar comparisons feature PG quasars at $z < 0.1$ (Shangguan et al. 2020) and bright ($L_{\rm bol} > 10^{44}{\rm ergs}^{-1}$) Hamburg/ESO quasars (Husemann et al. 2017). It is important to note that the selection criteria for PG quasars (Schmidt & Green 1983) and Hamburg/ESO quasars (Wisotzki et al. 2000) differ from those used for SDSS quasars (Richards et al. 2004).

In Fig. 9, in the right panel, we represent the ratio of molecular gas to stellar mass ($\mu_{\rm molgas}$) in different redshifts. Our dual quasars are represented by green stars. For J0847 and J1416, their host galaxies have already merged, resulting in a single M_* measurement for each, depicted as two green stars with black outlines. The comparison samples are depicted similarly to those in the left panel. For all samples, we use $R_{21} = 0.62$ and $\alpha_{\rm CO} = 3.1$. The bottom right error bars show uncertainties in $\mu_{\rm molgas}$ due to various choices of $\alpha_{\rm CO}$ and R_{21}. Solid lines indicate the best-fitting results of inactive galaxies from Tacconi et al. (2020). This fitting incorporates gas mass measurements of 2052 star-forming galaxies from the literature, covering redshifts from 0 to 5.2, stellar masses spanning $10^{9\text{–}12.2}\,{\rm M}_\odot$, and star formation rates (SFR) ranging from $10^{-1.5-3.75}\,{\rm M}_\odot\,{\rm yr}^{-1}$. The fitting function for the molecular gas-to-stellar mass ratio is based on redshift, relative specific star formation rate (sSFR), stellar mass, and effective radius:

$$\begin{aligned}\log \mu^{\rm gal}_{\rm molgas} &= A + B \times [\log(1+z) - F]^2 \\ &+ C \times \log[{\rm sSFR}/{\rm sSFR}\,({\rm MS}, z, M_*)] \\ &+ D \times [\log(M_*) - 10.7] \end{aligned} \quad (6)$$

We incorporate their optimal fit parameters $A = 0.06$, $B = -3.33$, $F = 0.65$, $C = 0.51$, $D = -0.41$ into the function. We define $\delta{\rm MS} = \log[{\rm sSFR}/{\rm sSFR}\,({\rm MS}, z, M_*)]$, and refer to this best-fitting result as $\mu^{\rm gal}_{\rm molgas}(z, \delta{\rm MS}, \log M_*)$.

The solid black line in Fig. 9 illustrates the galaxies of the star formation main sequence (SFMS), specifically $\mu^{\rm gal}_{\rm molgas}(z = 0\text{–}1, \delta{\rm MS} = 0, \log M_* = 10.7)$, where $\log\ M_*/{\rm M}_\odot = 10.7$ indicates the median mass of nearby galaxies (Saintonge et al. 2011), with the sSFR for SFMS galaxies defined by Speagle et al. (2014). By adjusting δMS to values of 1 and -1, we obtain the blue line for starburst (SB) galaxies and the red line for quiescent (QS) galaxies, respectively. From this figure, we find that most dual quasars exhibit a $\mu_{\rm molgas}$ comparable to SFMS galaxies, except for J1214N, which is an outlier above, and J2337S, which is an outlier below.

To compare the data while controlling for M_* as in Tacconi et al. (2018), we adjust $\mu_{\rm molgas}$ of our samples by relating them with $\mu^{\rm gal}_{\rm molgas}$ at the corresponding redshifts. We introduce:

$$\widetilde{\mu} = \mu/\mu({\rm MS}) \quad (7)$$

where μ is the observed $\mu_{\rm molgas}$ of the sources, and $\mu({\rm MS}) = \mu^{\rm gal}_{\rm molgas}(z = z_{\rm source}, \delta{\rm MS} = 0, \log M_* = 10.7)$. This method helps reduce redshift-dependent effects. The value $\widetilde{\mu}$ reflects the ratio of the sample's $\mu_{\rm molgas}$ to that of a typical medium-mass SFMS galaxy at the same redshift. Furthermore, equation (6) can be adjusted similarly, setting $\mu = \mu^{\rm gal}_{\rm molgas}(z = 0, \delta{\rm MS} = 0, \log M_* = 9.5 - 11.9)$ and $\mu({\rm MS}) = \mu^{\rm gal}_{\rm molgas}(z = 0, \delta{\rm MS} = 0, \log M_* = 10.7)$.[3]

We display $\widetilde{\mu}$ against $\log\ M_*$ in Fig. 10. The sample legends keep the same as those of Fig. 9. Distinctively, three pairs of dual quasars

[3]For any chosen z, provided that it is the same in both μ and μ(MS), the results are consistent. The range $\log M_* = 9.5 - 11.9$ is relevant for Fig. 10.

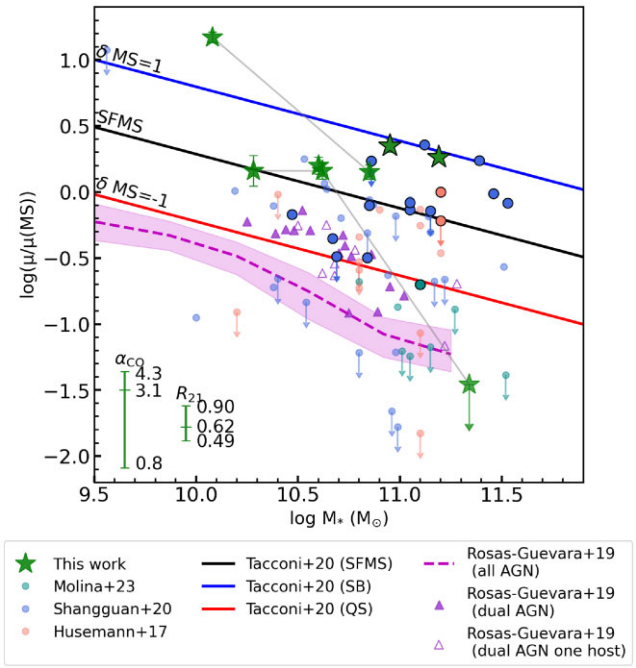

Figure 10. Normalized molecular gas-to-stellar mass ratio considering M_*. We define $\widetilde{\mu} = \mu/\mu({\rm MS}) = \mu_{\rm molgas}/\mu^{\rm gal}_{\rm molgas}(z = z_{\rm source}, \delta{\rm MS} = 0, \log {\rm M}_* = 10.7)$, representing the ratio of the source's $\mu_{\rm molgas}$ compared to medium-mass SFMS galaxies at an equivalent redshift. Sample legends are consistent with those in Fig. 9. Apart from the two pairs with a single host galaxy, we link the remaining three pairs with a line. In addition to the observational samples, the EAGLE simulation results (Rosas-Guevara et al. 2019) are included as dashed lines for the total AGN population and triangles for dual AGNs with either two host galaxies or one host galaxy, respectively.

are depicted as green stars linked by a grey line, except for the two pairs with a single host galaxy each. These dual quasars are treated as individual systems for which we estimate their combined $M_{\rm molgas}$, M_*, $\mu_{\rm molgas}$, and $\widetilde{\mu}$ in Table 4 columns (3–6). For the two non-detected companions, we incorporate their 3σ upper limits, which are minimal in effect compared to the systematic errors of the whole system. The error bars on the green stars in the figure reflect only the measurement errors of `imfit`. However, systematic uncertainties, mainly due to the choice of R_{21} and $\alpha_{\rm CO}$, as indicated by the green bars on the lower left, dominate the uncertainties of molecular gas measurement. We adopt 0.8 and 4.3 as the 2σ bounds for $\alpha_{\rm CO}$ and 0.49 and 0.90 for R_{21}. The values presented in Table 4 include both systematic and measurement errors.

To perform a comparison with the SFMS galaxies, we calculate $\widetilde{\mu}$ for the SFMS galaxies at the equivalent M_* for each pair of our dual quasars. This is expressed as $\widetilde{\mu}^{\rm SFMS}_{\rm molgas} = \mu^{\rm gal}_{\rm molgas}(z = z_{\rm source}, \delta{\rm MS} = 0, \log M_* = M_*^{\rm source})/\mu^{\rm gal}_{\rm molgas}(z = z_{\rm source}, \delta{\rm MS} = 0, \log M_* = 10.7)$. This can be perceived as projecting our samples vertically onto the black curve. The values are outlined in Table 4 column (7), with the uncertainties indicating $\delta{\rm MS} = \pm 1$. Consequently, Fig. 10 is partitioned into three regions: (1) 'SB-like': exceeding the upper threshold of $\widetilde{\mu}^{\rm SFMS}_{\rm molgas}$, or above the blue curve. (2) 'SFMS-like': within the range of the upper and lower threshold of $\widetilde{\mu}^{\rm SFMS}_{\rm molgas}$, or between the blue and red curves. (3) 'QS-like': beneath the red curve, below the red curves.

Next, we calculate the likelihood of $\widetilde{\mu}^{\rm dual}_{\rm molgas}$ residing in each of these three regions by assuming its probability density function (PDF)

Table 4. Molecular properties of our dual quasar systems are provided. Column (2) indicates the projected physical separation ($R_\perp$) between each pair, serving as an indicator of the merger stage. Columns (3) to (5) report the total molecular gas mass, stellar mass, and the molecular gas-to-stellar mass ratio for each pair. Column (6) presents the normalized total molecular gas-to-stellar mass ratio of each pair, defined as the relation between $\mu_{\rm molgas}$ and that of medium-mass SFMS galaxies at equivalent redshifts (refer to the text for further explanation). Column (7) details the normalized molecular gas-to-stellar mass ratio for SFMS galaxies matching in redshift and stellar mass to each dual quasar pair. Variations in $\delta{\rm MS} = \pm1$ within equation (6) set the lower and upper bounds. Column (8) enumerates the probabilities that $\widetilde{\mu}^{\rm dual}_{\rm molgas}$ falls above the upper bound (SB-like), within the bounds (SFMS-like), or below the lower bound (QS-like) of $\widetilde{\mu}^{\rm SFMS}_{\rm molgas}$.

Name	$R_\perp$	$\log\ M^{\rm dual}_{\rm molgas}$	$\log\ M^{\rm dual}_{*}$	$\mu^{\rm dual}_{\rm molgas}$	$\widetilde{\mu}^{\rm dual}_{\rm molgas}$	$\widetilde{\mu}^{\rm SFMS}_{\rm molgas}$	$P_{\widetilde{\mu}}$(SB, SFMS, QS)
	(kpc)	($M_\odot$)	($M_\odot$)	(%)	(ratio)	(ratio)	(%)
(1)	(2)	(3)	(4)	(5)	(6)	(7)	(8)
J0847	6.8	$10.72^{+0.11}_{-0.20}$	10.95 ± 0.16	$58.5^{+26.1}_{-34.8}$	$2.23^{+1.00}_{-1.33}$	$0.79^{+1.77}_{-0.55}$	37.0, 56.3, 6.7
J1214	13.3	$10.75^{+0.10}_{-0.20}$	10.92 ± 0.13	$68.5^{+26.4}_{-37.7}$	$3.39^{+1.31}_{-1.86}$	$0.81^{+1.82}_{-0.56}$	72.0, 23.4, 4.6
J1416	3.6	$10.70^{+0.10}_{-0.20}$	11.19 ± 0.13	$32.5^{+12.4}_{-17.8}$	$1.83^{+0.70}_{-1.00}$	$0.63^{+1.41}_{-0.44}$	38.2, 56.7, 5.1
J2209	9.0	$10.20^{+0.11}_{-0.20}$	10.78 ± 0.11	$26.3^{+9.5}_{-14.0}$	$1.44^{+0.52}_{-0.77}$	$0.92^{+2.07}_{-0.63}$	0.15, 93.1, 6.7
J2337	7.3	$10.33^{+0.11}_{-0.20}$	11.41 ± 0.12	$8.3^{+3.2}_{-4.5}$	$0.27^{+0.11}_{-0.15}$	$0.51^{+1.14}_{-0.35}$	0.0, 76.8, 23.2

follows a split normal distribution:

$$f\left(x;\mu,\sigma_{\rm low},\sigma_{\rm up}\right) = \begin{cases} A\exp\left(-\frac{(x-\mu)^2}{2\sigma^2_{\rm low}}\right), & \text{if } x < \mu \\ A\exp\left(-\frac{(x-\mu)^2}{2\sigma^2_{\rm up}}\right), & \text{otherwise} \end{cases} \quad (8)$$

where $A = \sqrt{2/\pi}\left(\sigma_{\rm low} + \sigma_{\rm up}\right)^{-1}$, $\sigma_{\rm low}$ and $\sigma_{\rm up}$ are the lower and upper 1σ uncertainty as shown in Table 4 column (6) for each system, respectively. Subsequently, we determine the area (i.e. probabilities) of this PDF within 'SB-like', 'SFMS-like', or 'QS-like' regions, which are referred as $P_{\widetilde{\mu}}$ and presented in Table 4, column (8). Consequently, four out of our five dual quasar systems exhibit a probability of less than 7 per cent of being QS-like, with the remaining system showing a probability of 23 per cent. Thus, we conclude that, during the merger phase with an approximate separation of 10 kpc, our dual quasars as a collective do not provide substantial evidence of cold molecular gas being significantly depleted. Furthermore, we find the $\widetilde{\mu}$ values for our dual quasars are similar to those single AGNs in mergers (Husemann et al. 2017; Shangguan et al. 2020; Molina et al. 2023, the larger coloured dots with black edges in Fig. 10). These pieces of evidence may imply that no matter with single or dual AGNs in effect, the gas depletion time-scale exceeds the merging dynamical time-scale (Capelo et al. 2015), and most gas become depleted after the final merger (Hopkins et al. 2006). None the less, certain individual quasars within these dual systems do demonstrate minimal or absent CO-emitting gas. The data in this study are yet limited in statistical power, and additional follow-up observations of dual quasars with varying separations are needed to evaluate the gas depletion hypothesis.

In addition to the observational data, we incorporate the EAGLE simulation results (Rosas-Guevara et al. 2019) for comparison. The complete AGN population from the simulation, covering the redshift range z = 0.8–1.0, is represented by the magenta dashed line with a 1σ distribution. The simulated dual AGNs with two host galaxies are depicted as filled triangles, while those with a single host galaxy are shown as open triangles. They observed that most dual AGN systems are relatively gas-richer than the entire AGN population. Our observations corroborate this, as contrasted with the single quasars in Husemann et al. (2017), Shangguan et al. (2020), and Molina et al. (2023), but with an overall excess of ∼0.5 dex in $\widetilde{\mu}$ over the dual AGNs in the EAGLE simulation. It is important to highlight that EAGLE defines AGNs based on 2–10 keV X-ray luminosities exceeding 10^{42}erg s^{-1}, approximately 1–2 dex fainter in $L_{\rm bol}$ compared to our dual quasars (Table A1). Due to selection bias, our dual quasars likely represent an extreme population that is not yet widely replicated by current simulations.

4.2 J1214N: merger or disc?

In Section 3.2.2 and Fig. 5, we emphasized the gradient feature detected in the velocity map of J1214N. We explore possible interpretations for this structure. Primarily, the v/σ ratio being nearly one suggests that a merger is taking place, as supported by numerical simulations (such as Lapi et al. 2018) and observations of local dual AGNs (e.g. Feruglio et al. 2013). The merger front is likely oriented along the minor axis of the CO M1 map of J1214N [refer to Fig. 5 panel (b)]. Furthermore, the HSC image uncovers another red galaxy to the northwest of J1214N, positioned 2.0 arcsec or 8.4 kpc away [see Fig. 5 panel (a)]. Despite the absence of spectroscopic data, the image displays tidal interactions between this galaxy and J1214N. Its lack of detection by ALMA implies that it could be a quiescent galaxy if at the same redshift. Consequently, the system might exist within a densely packed region approximately 20 kpc in scale.

Biconical outflows driven by AGN feedback are capable of generating double-peaked emission lines and velocity gradient features within the molecular and ionized gas phases (Cicone et al. 2014; Comerford et al. 2018). However, these outflows generally create asymmetric line profiles, probably due to the asymmetric geometry of the outflow bicone (Nevin et al. 2018). For J1214N, the CO emission line presents nearly identical peaks [Fig. 5 panel (g)], which contradicts the typical asymmetry associated with an outflow scenario. Furthermore, galaxy mergers often lead to asymmetric line profiles, as the two interacting galaxies usually exhibit different brightness levels (Maschmann et al. 2020).

Thus, despite being shown unfavorable by the v/σ ratio, we explore the possibility of a rotating disc in an alternative scenario, which is recognized for generating symmetric double-peaked emission lines (Storchi-Bergmann et al. 2017; Maschmann et al. 2020, 2023). To verify this hypothesis, we conduct a kinematic evaluation of this aspect using the tool 3D-Based Analysis of Rotating Objects via Line Observations ($^{\rm 3D}$ Barolo, Teodoro & Fraternali 2015). Essentially, $^{\rm 3D}$Barolo fits a rotating disc model with a series of concentric rings, utilizing emission line data cubes. This tool is widely applied in the study of galaxy gas kinematics (e.g. Ginolfi et al. 2020; Maddox et al. 2021). We exclude J1214S from the modelling process, which would otherwise be integrated as part of the disc. The `SEARCH` function of $^{\rm 3D}$ Barolo operates on DUCHAMP (Whiting 2012), producing a 3D source mask. We set the `SNRCUT` for detection to 7, `GROWTHCUT`

to 4, and MINCHANNELS to 4 to ensure only J1214N remains in the model while minimizing noise pixels. Subsequently, we apply the imfit results of the M0 map to refine the model, consistent with the approach by Banerji et al. (2021). We anchor the model centre (XPOS and YPOS) and position angle (PA) to the imfit results, then determine the ring model parameters accordingly:

$$\mathrm{NRADII} = \mathrm{round}\left(\frac{\mathrm{FWHM_{major}}}{\mathrm{FWHM_{minor}}/2.5}\right) \quad (9)$$

$$\mathrm{RADSEP} = \frac{\mathrm{FWHM_{major}}}{\mathrm{NRADII}} \quad (10)$$

In this context, NRADII denotes the number of rings, specifically 7 for our study, while RADSEP represents the separation (width) between these rings, valued at 0.187. These parameters are crucial to ensure that the fitting process concentrates on the central region, avoiding excessive resolution of the data and minimizing extraneous noise. We consider rotation velocity (VROT), velocity dispersion (VDISP), inclination angle (INC), and the disc's scale-height (Z0) as free parameters, starting with initial estimates derived from the M1 and M2 maps (VROT = 200, VDISP = 40, INC = 71, Z0 = 0). Specifically, for the inclination angle, the initial value is computed based on the galaxy's axial ratio as outlined by Holmberg (1958):

$$\mathrm{INC} = \cos^{-1}\left(\sqrt{\frac{q^2 - q_0^2}{1 - q_0^2}}\right) \quad (11)$$

where q is the ratio of the semi-minor to the semi-major axis of the galaxy (i.e. $\mathrm{FWHM_{minor}}/\mathrm{FWHM_{major}}$) achieved from imfit, q0 is assumed to be 0.2 (Pierce & Tully 1988).

Ultimately, the inclination angle stabilizes at 75.4 deg. To verify this, we compared results from a 2D decomposition on the Subaru/HSC i-band image using GALIGHT (Ding et al. 2022), yielding $q = 0.31$, or INC = 76 deg for J1214N. Fig. 11 displays the ^{3D}Barolo model and residuals. From top to bottom are the intensity (M0), velocity (M1), and dispersion (M2) maps. Each column from left to right corresponds to observational data, fitted models, and residuals. The optimal fit indicates a nearly uniform VROT $\sim 225\,\mathrm{km\,s^{-1}}$ across the rings. Once instrumental broadening is subtracted ($\sigma_{\mathrm{instr}} = W_{\mathrm{ch}}/\sqrt{2\ln 2}$ as defined in ^{3D}Barolo, with a channel width of $10\,\mathrm{km\,s^{-1}}$ in our case), velocity dispersion declines approximately linearly from $32\,\mathrm{km\,s^{-1}}$ at the innermost ring to $4\,\mathrm{km\,s^{-1}}$ at the second outermost ring. Details of the density profile from the best-fitting model appear in Table 5.

With VROT and the size of the major axis (a_{major}, Table 3 column 6), we calculate the dynamical mass of J1214N with the following formula:

$$\left(\frac{M_{\mathrm{dyn}}}{\mathrm{M_\odot}}\right) = 1.16 \times 10^5 \left(\frac{\mathrm{VROT}}{\mathrm{km\ s^{-1}}}\right)^2 \left(\frac{1.5 \times a_{\mathrm{major}}}{\mathrm{kpc}}\right) \quad (12)$$

A factor of 1.5 was utilized to account for the disc's faint emissions (refer to Wang et al. 2013; Izumi et al. 2021). Consequently, the dynamic mass for J1214N was estimated as $M_{\mathrm{dyn}} \sim 10^{10.84}\,\mathrm{M_\odot}$. Assuming $M_{\mathrm{dyn}} = M_{\mathrm{gas}} + M_* + M_{\mathrm{BH}}$, we estimated $M_{\mathrm{gas}} = 10^{10.56}\,\mathrm{M_\odot}$. For comparison, our measurements from CO J = 2–1 suggest a molecular gas mass of $M_{\mathrm{molgas}} \sim 10^{10.45}\,\mathrm{M_\odot}$, accounting for approximately 77.6 per cent of the total gas mass.

In the examination of the source's M2 map, a notable blob is identified approximately 1 arcsec north-west of J1214N, exhibiting a velocity dispersion of about $110\,\mathrm{km\,s^{-1}}$ (Fig. 11, bottom left panel). This feature conflicts with the expected outcomes of a rotating disc model, which generally shows dispersion concentrating near the centre of the M0 map (Fig. 11, bottom middle panel). Discrepancies are evident in the residual map (Fig. 11, bottom right panel). Such findings support the merger scenario for J1214N. Nevertheless, we cannot completely discard the disk model with the current observational resolution. Thus, we plan to perform higher resolution and multiwavelength observations in the future to further elucidate the nature of this source.

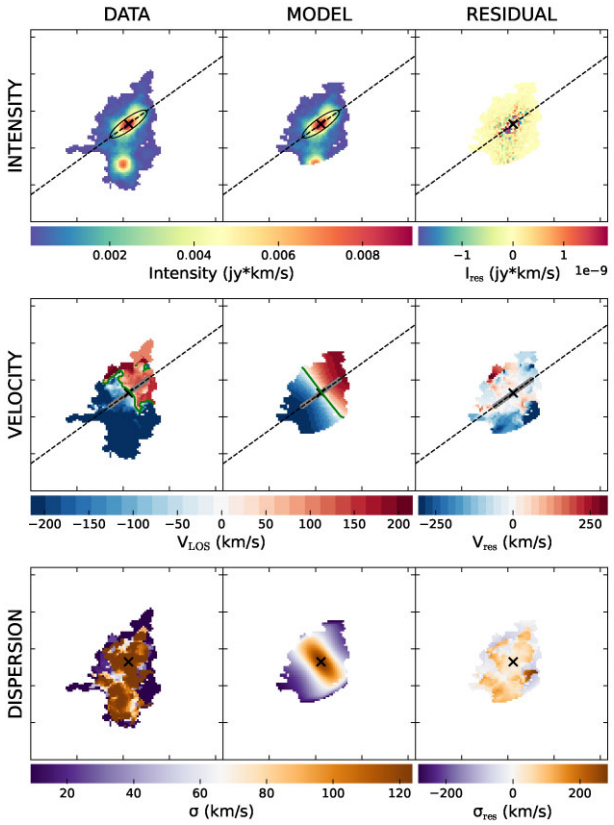

Figure 11. ^{3D}Barolo output results for J1214 are organized in the maps M0, M1, and M2 from top to bottom. Displayed from left to right are the observed data, the fitting model, and the residuals. Black crosses indicate the centre of the disc model. The fitting includes only the northern sources, delineated by the black elliptical aperture. Dashed lines show the major axis orientation.

Table 5. ^{3D} Barolo density profiles for J1214N feature a best-fitting model comprising seven rings, each spaced at a constant 0.187 arcsec. Column (1) lists the ring radius in arcsec. Column (2) provides the median flux and its median absolute deviation, measured in $\mathrm{mJy \cdot km \cdot s^{-1}}$. Column (3) indicates the count of valid pixels in each ring. Column (4) shows the ring's surface density, expressed in $\mathrm{mJy \cdot km \cdot s^{-1}\ arcsec^{-2}}$.

Radius (arcsec) (1)	$< F >$ ($\mathrm{mJy \cdot km \cdot s^{-1}}$) (2)	N_{pix} # (3)	Φ ($\mathrm{mJy \cdot km \cdot s^{-1}\ arcsec^{-2}}$) (4)
0.094	9.2 ± 0.2	2	916 ± 30
0.280	8.7 ± 0.5	9	835 ± 82
0.468	7.3 ± 0.8	13	734 ± 99
0.655	6.1 ± 0.9	20	628 ± 124
0.842	4.7 ± 1.0	26	500 ± 139
1.029	3.8 ± 1.3	31	400 ± 157
1.215	3.0 ± 1.4	37	312 ± 160

4.3 Insights on galaxy evolution

In our study, our aim was to extract insights related to the expansive field of galaxy evolution, concentrating particularly on the interplay between galaxy mergers and quasars. The traditional evolutionary model suggests that gas-rich major mergers play a pivotal role in initiating quasar activity (Hopkins et al. 2008). However, numerous observational studies have since sparked extensive discussions (e.g. Gabor et al. 2009; Cisternas et al. 2010; Silverman et al. 2011; Boehm et al. 2013; Villforth et al. 2014, 2017; Ellison et al. 2019; Marian et al. 2019, 2020; Zhao et al. 2022). The complexities arise from multiple elements, notably the criteria used to select quasars, such as considering their spectral range, brightness, redshift, and the variety of techniques used to classify mergers (e.g. visual assessment, morphological indicators, machine learning).

This underscores the benefits of researching dual quasars: They are clearly identified mergers, their merger stages being probed by the separations between the two optical nuclei. Furthermore, there are data available on the SMBH properties for both galaxies, placing them within a well-defined framework for discussing the coevolution scenario. We begin by reviewing the features of our dual quasar sample. Their bolometric luminosities, deduced from their 5100 Å monochromatic luminosities, range from 10^{44} to $10^{45.5}$ erg s^{-1}, situating them at the dim end of the quasar luminosity function at $z \sim 1$ (Shen et al. 2020). Both the black hole and host galaxy masses are comparable to those in the parent SDSS DR14 quasar sample (Tang et al. 2021). To gauge the representativeness of this phase, we examined the overall merger fraction for SDSS-HSC cross-matched quasars within this luminosity range at $0.2 < z < 0.8$ (Tang et al. 2023). Using the morphological method of this study, the general fraction of quasar merger is between 10 per cent and 25 per cent. The Horizon-AGN simulation estimates that a dual AGN fraction (among all AGN) with $L_{\rm bol} > 10^{44}$ erg s^{-1}, $R_{\perp} < 30$ kpc and $z \sim 0.5$ to be approximately 2 per cent (Volonteri et al. 2022), suggesting that our dual quasars may represent a stage accounting for 8 per cent–20 per cent of a quasar's lifecycle during a merger event.

In Section 4.1, we evaluated the overall molecular gas content of each pair of quasars, comparing it with single quasars and inactive galaxies. Our analysis reveals no substantial differences among these groups. Therefore, the presence of two active quasars does not appear to significantly alter the global gas environment. Subsequently, we examine whether the molecular gas in each quasar shows any preferential alignment with the properties of the black holes. For instance, is the molecular gas consistently associated with SMBH which is more luminous ($L_{\rm bol}$), more massive ($M_{\rm BH}$), or more actively accreting ($\lambda_{\rm Edd}$) SMBH? In the cases of J1416 and J2337, CO detections are observed in only one member of the pair. The detected J1416W correlates with the brighter, more massive, and less actively accreting counterpart, while J2337N corresponds with the dimmer, less massive, and more actively accreting counterpart. The findings appear to be arbitrary, show no definitive preference related to the SMBH characteristics.

AGN feedback is generally recognized as a self-regulating mechanism that modulates the balance between SMBH and its surroundings [(see reviews by Fabian (2012) and Morganti (2017)]. Thus, it is understandable that no correlation is observed between molecular gas quantities and transient properties like $L_{\rm bol}$ and $\lambda_{\rm Edd}$. In contrast, as a long-term characteristic, $M_{\rm BH}$ is more apt to show correlations with the overall molecular gas content in quasars. This correlation is also logically expected from the intersection of the $M_{\rm BH}$–M_* relationship (Kormendy & Ho 2013) and the M_*–SFR relationship (Davé 2008). None the less, due to the significant uncertainties in the virial methods used for $M_{\rm BH}$ measurement and the conversion factors for molecular gas mass, a larger sample size is needed to substantiate any claimed correlation.

We investigate whether the asymmetric distribution of molecular gas could be attributed to the effects of the merger. Specifically, is it possible that one of the SMBHs is capturing most of the system's molecular gas through the interaction? To delve into this theory, we analyse the evolutionary paths of comparable systems in hydrodynamical simulations. Capelo et al. (2015) studied the evolution of physical characteristics of SMBHs and their host galaxies during mergers, ranging from a chaotic phase well before galaxy interaction to a remnant stage after the BHs merge beneath the stellar softening length. Notably, Capelo et al. (2015) tracked gas mass at distances of 0.1, 1, and 10 kpc around the primary and secondary BHs in galaxy mergers. For a BH mass ratio of 1:4, their simulations indicate that the total gas content (within 1 or 10 kpc radius, similar to the scales we focus on) stayed nearly unchanged for both BHs throughout the entire merger. Consistent findings were reported in their simulations of a 1:2 merger, where the overall gas volumes were minimally impacted during the merger. Thus, we infer that the presence or absence of gas detection in our dual quasars likely reflects the inherent properties of each galaxy before reaching their present condition. However, it is important to emphasize that our detection threshold for $M_{\rm molgas}$ slightly exceeds 10^9 M$_\odot$, the boundary for classifying 'gas-poor' and 'non-detection' in this study.

5 CONCLUSIONS

In this study, we present the results of the use of ALMA to observe cold molecular gas (CO J = 2–1) in five proximate dual quasars with $R_{\perp} < 20$ kpc and $L_{\rm bol} \gtrsim 10^{44}$ erg s^{-1} within the redshift range $0.4 < z < 0.8$. The key outcomes are outlined as follows.

(i) CO J = 2–1 line detections above 5σ have been observed in eight out of 10 quasars in the five dual systems, with $S_{\rm CO(2\text{-}1)} > 0.5$ mJy. These findings collectively point to an expected molecular gas mass ($M_{\rm molgas}$) range from $10^{9.7\text{–}10.7}$ M$_\odot$, assuming $R_{21} = 0.62$ and $\alpha_{\rm CO} = 3.1$. Source sizes are determined from the moment 0 map. Among the eight detected sources, five of them have CO emitting regions spanning over 1.5 beam sizes. (See Fig. 3 and Table 3).

(ii) The molecular gas distribution in these dual quasars reveals varied characteristics: J0847 has a displaced gas blob 8.2 kpc away from the optical centre; J1214N shows a distinct velocity gradient, indicating either a merger or a rotating disc; J1416, the sole type1–type1.5 pair in this study, has CO gas detected only in the obscured companion. In contrast, J2337, a type1–type1 pair, also exhibits CO gas detection only in one of the companions (Section 3.2).

(iii) A logrank test comparing the CO luminosities ($L'_{\rm CO(2\text{-}1)}$) between our dual quasars and single quasars at similar redshifts does not reveal significant statistical differences (Fig. 9).

(iv) When evaluating each pair as a singular entity, their total molecular to stellar mass ratios ($\mu^{\rm dual}_{\rm molgas}$) range from 8 per cent to 70 per cent. Adjusting for redshift dependence, their normalized gas ratios ($\widetilde{\mu}$) vary from approximately 0.3 to 3.4 times that of typical star-forming galaxies on the main sequence. Taking into account both measurement and systemic errors, each pair's $\widetilde{\mu}$ has a minimum 75 per cent chance of exceeding that of quiescent galaxies with an equivalent stellar mass (Table 4).

(v) The $\widetilde{\mu}$ values for dual quasars closely match those of single quasars involved in mergers, suggesting that an additional AGN has an insignificant feedback impact in these systems, as the gas depletion time scale might be longer than the dynamical time-scale

(Section 4.1). We also do not find significant correlations between $\widetilde{\mu}$ and the BH properties of each pair (Section 4.3).

In summary, the molecular gas environments of dual quasars are rich and diverse, even within a narrow parameter space and uniform selection. The two main questions that remain are: (1) At which stage of galaxy mergers will the molecular gas be depleted? (2) What are the underlying physical mechanisms driving the diversity in molecular gas distribution? To address these questions, a larger sample across different redshifts and with various separations needs to be observed using multiwavelength and high-resolution techniques. Combining a broader range of observational data with simulations will provide deeper insights into these phenomena.

ACKNOWLEDGEMENTS

This paper makes use of the following ALMA data: ADS/JAO.ALMA#2021.1.01233.S ALMA is a partnership of ESO (representing its member states), NSF (USA) and NINS (Japan), together with NRC (Canada), MOST and ASIAA (Taiwan), and KASI (Republic of Korea), in cooperation with the Republic of Chile. The Joint ALMA Observatory is operated by ESO, AUI/NRAO and NAOJ.

ST and MB acknowledge funding from the Royal Society via a University Research Fellowship to MB and associated Research Fellows Enhancement Awards. CB gratefully acknowledges support from the Forrest Research Foundation. Special thanks go to the East Asian ALMA Regional Center (EA ARC) and the UK ALMA Regional Centre (UK ARC) nodes for their responsive support on the data achievement and processing of this work. ST is grateful to Dr. Dan Walker for the suggestions on `imfit`, Dr. Annagrazia Puglisi and Dr. Sebastien Muller for their suggestions on dealing with the *uv* data, Dr. Wenke Ren for the suggestions on PYQSOFIT, and Dr. Xuheng Ding for the suggestions on GALIGHT. The authors thank the anonymous referee for their valuable comments that significantly helped to improve this manuscript.

DATA AVAILABILITY

The raw data is public on ALMA archive with project ID: 2021.1.01233.S. The reprocessed ALMA data and the photometric fitting results of all sources are available in the online supplementary material of this paper.

REFERENCES

Aihara H. et al., 2022, PASJ, 74, 247
Akaike H., 1998, Selected papers of hirotugu akaike. New York, NY, Springer New York, p. 199
Anguita T. et al., 2018, MNRAS, 480, 5017
Banerji M., Carilli C., Jones G., Wagg J., McMahon R., Hewett P., Alaghband-Zadeh S., Feruglio C., 2017, MNRAS, 465, 4390
Banerji M., Jones G. C., Carniani S., DeGraf C., Wagg J., 2021, MNRAS, 503, 5583
Bean B. et al., 2022, PASP, 134, 114501
Bertin E., 2013, Astrophysics Source Code Library, record ascl:1301.
Boehm A. et al., 2013, A&A, 549, A46
Bolatto A. D., Wolfire M., Leroy A. K., 2013, ARA&A, 51, 207
Boquien M., Burgarella D., Roehlly Y., Buat V., Ciesla L., Corre D., Inoue A., Salas H., 2019, A&A, 622, A103
Bosch J. et al., 2018, PASJ, 70, S5
Bradley L. et al., 2024, astropy/photutils: 1.12.0. Zenodo
Briggs D., 1995, in American Astronomical Society Meeting Abstracts Vol. 187. p. 112
Bruzual G., Charlot S., 2003, MNRAS, 344, 1000
Calzetti D., Armus L., Bohlin R. C., Kinney A. L., Koornneef J., Storchi-Bergmann T., 2000, ApJ, 533, 682
Capelo P. R., Volonteri M., Dotti M., Bellovary J. M., Mayer L., Governato F., 2015, MNRAS, 447, 2123
Capelo P. R., Dotti M., Volonteri M., Mayer L., Bellovary J. M., Shen S., 2017, MNRAS, 469, 4437
Carilli C., Walter F., 2013, ARA&A, 51, 105
Carniani S. et al., 2017, A&A, 605, A105
Chabrier G., 2003, PASP, 115, 763
Chan J. H. et al., 2020, A&A, 636, A87
Charlot S., Fall S. M., 2000, ApJ, 539, 718
Chen Y.-C., Hwang H.-C., Shen Y., Liu X., Zakamska N. L., Yang Q., Li J. I., 2022, ApJ, 925, 162
Chen Y.-C. et al., 2023, Nature, 616, 45
Chen Y.-C. et al., 2024, ApJ, 968, 9
Cicone C. et al., 2014, A&A, 562, A21
Cisternas M. et al., 2010, ApJ, 726, 57
Ciurlo A. et al., 2023, A&A, 671, 6
Comerford J. M., Pooley D., Gerke B. F., Madejski G. M., 2011, ApJ, 737, L19
Comerford J. M., Pooley D., Barrows R. S., Greene J. E., Zakamska N. L., Madejski G. M., Cooper M. C., 2015, ApJ, 806, 219
Comerford J. M., Nevin R., Stemo A., Müller-Sánchez F., Barrows R. S., Cooper M. C., Newman J. A., 2018, ApJ, 867, 66
Comrie A. et al., 2021, Astrophysics Source Code Library, record ascl: 2103.
Cornwell T. J., 2008, IEEE J. Sel. Top. Signal Proc, 2, 793
Dale D. A., Helou G., Magdis G. E., Armus L., Díaz-Santos T., Shi Y., 2014, ApJ, 784, 83
Davé R., 2008, MNRAS, 385, 147
Davis T. A. et al., 2011, MNRAS, 414, 968
De Rosa A. et al., 2019, New Astron. Rev., 86, 101525
Decarli R. et al., 2017, Nature, 545, 457
Di Matteo T., Springel V., Hernquist L., 2005, nature, 433, 604
Di Matteo T., Colberg J., Springel V., Hernquist L., Sijacki D., 2008, ApJ, 676, 33
Ding X., Silverman J., Birrer S., Treu T., Tang S., Yang L., Bottrell C., 2022, Astrophysics Source Code Library, record: ascl:2209.011
Ding X. et al., 2023, Nature, 621, 51
Downes D., Solomon P., 1998, ApJ, 507, 615
Eftekharzadeh S., Myers A., Hennawi J., Djorgovski S., Richards G., Mahabal A., Graham M., 2017, MNRAS, 468, 77
Ellison S. L., Viswanathan A., Patton D. R., Bottrell C., McConnachie A. W., Gwyn S., Cuillandre J.-C., 2019, MNRAS, 487, 2491
Fabian A. C., 2012, ARA&A, 50, 455
Feruglio C., Fiore F., Piconcelli E., Cicone C., Maiolino R., Davies R., Sturm E., 2013, A&A, 558, A87
Fu H. et al., 2011, ApJ, 740, L44
Fu H., Wrobel J., Myers A., Djorgovski S., Yan L., 2015, ApJ, 815, L6
Fujimoto S. et al., 2020, ApJ, 900, 1
Gabor J. et al., 2009, ApJ, 691, 705
Gilks W. R., Richardson S., Spiegelhalter D., 1995, Markov chain Monte Carlo in practice.CRC Press, Florida, United States
Ginolfi M. et al., 2020, A&A, 633, A90
Glikman E. et al., 2023, ApJ, 951, L18
Goulding A. D., Pardo K., Greene J. E., Mingarelli C. M., Nyland K., Strauss M. A., 2019, ApJ, 879, L21
Green P. J., Myers A. D., Barkhouse W. A., Aldcroft T. L., Trichas M., Richards G. T., Ruiz Á., Hopkins P. F., 2011, ApJ, 743, 81
Guo H., Shen Y., Wang S., 2018, Astrophysics Source Code Library, record ascl: 1809
Guo H., Liu X., Shen Y., Loeb A., Monroe T., Prochaska J. X., 2019, MNRAS, 482, 3288
Hennawi J. F. et al., 2006, AJ, 131, 1
Hennawi J. F. et al., 2010, ApJ, 719, 1672
Holmberg E., 1958, Meddelanden fran Lunds Astronomiska Observatorium Serie II, 136, 1

Hopkins P. F., Hernquist L., Cox T. J., Di Matteo T., Robertson B., Springel V., 2006, ApJS, 163, 1
Hopkins P. F., Hernquist L., Cox T. J., Kereš D., 2008, ApJS, 175, 356
Husemann B., Davis T., Jahnke K., Dannerbauer H., Urrutia T., Hodge J., 2017, MNRAS, 470, 1570
Inada N. et al., 2008, AJ, 135, 496
Inada N. et al., 2012, AJ, 143, 119
Inoue A. K., 2011, MNRAS, 415, 2920
Ishikawa Y. et al., 2024, ApJ, 982, 17
Izumi T. et al., 2018, PASJ, 70, 36
Izumi T. et al., 2020, ApJ, 898, 61
Izumi T. et al., 2021, ApJ, 914, 36
Jones G. et al., 2017, ApJ, 850, 180
Kapferer W., Kronberger T., Ferrari C., Riser T., Schindler S., 2008, MNRAS, 389, 1405
Kayo I., Oguri M., 2012, MNRAS, 424, 1363
Kennedy J., Eberhart R., 1995, in Proceedings of ICNN'95-international conference on neural networks. Vol. 4. ieee 1995, Seattle, Washington, p.1942
Kormendy J., Ho L. C., 2013, ARA&A, 51, 511
Koss M., Mushotzky R., Treister E., Veilleux S., Vasudevan R., Trippe M., 2012, ApJ, 746, L22
Koss M. J. et al., 2023, ApJ, 942, L24
Krips M., Neri R., Cox P., 2012, ApJ, 753, 135
Lapi A. et al., 2018, ApJ, 857, 22
Lavezzi T., Dickey J., 1997, AJ, 114, 2437
Lemon C. A., Auger M. W., McMahon R. G., Ostrovski F., 2018, MNRAS, 479, 5060
Lemon C. A., Auger M. W., McMahon R. G., 2019, MNRAS, 483, 4242
Lemon C. et al., 2020, MNRAS, 494, 3491
Lemon C., Millon M., Sluse D., Courbin F., Auger M., Chan J., Paic E., Agnello A., 2022, A&A, 657, A113
Lemon C. et al., 2023, MNRAS, 520, 3305
Li J., Zhuang M.-Y., Shen Y., 2024, ApJ, 961, 19
Liu X., Shen Y., Strauss M. A., Hao L., 2011, ApJ, 737, 101
Maddox N. et al., 2021, A&A, 646, A35
Maiolino R. et al., 2023, A&A, 691, 29
Mannucci F. et al., 2023, A&A, 680, 13
Mantel N., et al., 1966, Cancer Chemother Rep, 50, 163
Maraston C., 2005, MNRAS, 362, 799
Marian V. et al., 2019, ApJ, 882, 141
Marian V. et al., 2020, ApJ, 904, 79
Maschmann D., Melchior A.-L., Mamon G. A., Chilingarian I. V., Katkov I. Y., 2020, A&A, 641, A171
Maschmann D., Halle A., Melchior A.-L., Combes F., Chilingarian I. V., 2023, A&A, 670, A46
Matsuoka Y. et al., 2024, ApJ, 965, L4
Molina J., Shangguan J., Wang R., Ho L. C., Bauer F. E., Treister E., 2023, ApJ, 950, 60
Molyneux S. et al., 2024, MNRAS, 527, 4420
More A. et al., 2016, MNRAS, 456, 1595
Morganti R., 2017, Front. Astron. Space Sci, 4, 42
Müller-Sánchez F., Comerford J. M., Nevin R., Barrows R. S., Cooper M. C., Greene J. E., 2015, ApJ, 813, 103
Myers A. D., Richards G. T., Brunner R. J., Schneider D. P., Strand N. E., Hall P. B., Blomquist J. A., York D. G., 2008, ApJ, 678, 635
Nevin R., Comerford J. M., Müller-Sánchez F., Barrows R., Cooper M. C., 2018, MNRAS, 473, 2160
Nguyen N. H., Lira P., Trakhtenbrot B., Netzer H., Cicone C., Maiolino R., Shemmer O., 2020, ApJ, 895, 74
Owen F. N., O'Dea C. P., Inoue M., Eilek J. A., 1985, ApJ, 294, L85
Pâris I. et al., 2018, A&A, 613, A51
Perna M. et al., 2023, A&A, 679, 23
Pierce M. J., Tully R. B., 1988, ApJ, 330, 579
Pozzi F. et al., 2024, A&A, 686, A187
Ren W., Guo H., Shen Y., Silverman J. D., Burke C. J., Wang S., Wang J., 2024, ApJ, 974, 153
Richards G. T. et al., 2004, ApJS, 155, 257
Richards G. T. et al., 2006, ApJS, 166, 470
Rosas-Guevara Y. M., Bower R. G., McAlpine S., Bonoli S., Tissera P. B., 2019, MNRAS, 483, 2712
Saintonge A. et al., 2011, MNRAS, 415, 32
Sanders D., Mirabel I., 1996, ARA&A, 34, 749
Schmidt M., Green R. F., 1983, ApJ, 269, 352
Scholtz J., Maiolino R., Jones G., Carniani S., 2023, MNRAS, 519, 5246
Schulze A. et al., 2018, ApJS, 239, 22
Schulze A. et al., 2019, MNRAS, 488, 1180
Schwarz G., 1978, Ann. Stat., 6, 461
Scialpi M. et al., 2023, A&A, 690, 16
Shangguan J., Ho L. C., Bauer F. E., Wang R., Treister E., 2020, ApJS, 247, 15
Shao Y. et al., 2017, ApJ, 845, 138
Shen Y., 2013, Bull. Astron. Soc. India, 41, 61
Shen Y. et al., 2011, ApJS, 194, 45
Shen X., Hopkins P. F., Faucher-Giguère C.-A., Alexander D., Richards G. T., Ross N. P., Hickox R., 2020, MNRAS, 495, 3252
Shen Y. et al., 2021, Nat. Astron., 5, 569
Silverman J. et al., 2011, ApJ, 743, 2
Silverman J. D. et al., 2020, ApJ, 899, 154
Solomon P., Downes D., Radford S., 1992, ApJ, 398, L29
Speagle J. S., Steinhardt C. L., Capak P. L., Silverman J. D., 2014, ApJS, 214, 15
Steinborn L. K., Dolag K., Comerford J. M., Hirschmann M., Remus R.-S., Teklu A. F., 2016, MNRAS, 458, 1013
Storchi-Bergmann T., Schimoia J. d. S., Peterson B. M., Elvis M., Denney K. D., Eracleous M., Nemmen R. S., 2017, ApJ, 835, 236
Tacconi L. J. et al., 2018, ApJ, 853, 179
Tacconi L. J., Genzel R., Sternberg A., 2020, ARA&A, 58, 157
Tan Q.-H. et al., 2024, A&A, 684, A23
Tang S. et al., 2021, ApJ, 922, 83
Tang S. et al., 2023, MNRAS, 521, 5272
Teodoro E. D., Fraternali F., 2015, MNRAS, 451, 3021
Tiley A. L., Bureau M., Saintonge A., Topal S., Davis T. A., Torii K., 2016, MNRAS, 461, 3494
Treister E., Natarajan P., Sanders D. B., Urry C. M., Schawinski K., Kartaltepe J., 2010, Science, 328, 600
Übler H. et al., 2024, MNRAS, 531, 355
Valentini M. et al., 2020, MNRAS, 491, 2779
Van Wassenhove S., Volonteri M., Mayer L., Dotti M., Bellovary J., Callegari S., 2012, ApJ, 748, L7
Venemans B. P. et al., 2017, ApJ, 837, 146
Vestergaard M., Peterson B. M., 2006, ApJ, 641, 689
Villforth C. et al., 2014, MNRAS, 439, 3342
Villforth C. et al., 2017, MNRAS, 466, 812
Volonteri M., Dubois Y., Pichon C., Devriendt J., 2016, MNRAS, 460, 2979
Volonteri M., Pfister H., Beckmann R., Dotti M., Dubois Y., Massonneau W., Musoke G., Tremmel M., 2022, MNRAS, 514, 640
Walter F. et al., 2022, ApJ, 927, 21
Wang R. et al., 2013, ApJ, 773, 44
Whiting M. T., 2012, MNRAS, 421, 3242
Willott C. J., Bergeron J., Omont A., 2017, ApJ, 850, 108
Wisotzki L., Christlieb N., Bade N., Beckmann V., Köhler T., Vanelle C., Reimers D., 2000, A&A, 358, 77
Woo J.-H., Cho H., Husemann B., Komossa S., Park D., Bennert V. N., 2014, MNRAS, 437, 32
Xia X. et al., 2012, ApJ, 750, 92
Yue M. et al., 2021a, ApJ, 917, 99
Yue M., Fan X., Yang J., Wang F., 2021b, ApJ, 921, L27
Zhao Y., Li Y. A., Shangguan J., Zhuang M.-Y., Ho L. C., 2022, ApJ, 925, 70

SUPPORTING INFORMATION

Supplementary data are available at *MNRAS* online.

Figure 2. Photometric evaluations conducted with GALIGHT and CIGALE on J1214.

Please note: Oxford University Press is not responsible for the content or functionality of any supporting materials supplied by the authors. Any queries (other than missing material) should be directed to the corresponding author for the article.

APPENDIX A: OPTICAL SPECTRA FITTING

The optical spectra fitting for the five dual quasars reported in this paper are detailed in Silverman et al. (2020) and Tang et al. (2021). In this work, we have re-analysed the spectroscopic data using the PYTHON-based QSO fitting tool (PYQSOFIT; Guo, Shen & Wang 2018). The results of these fits are shown in Fig. A1.

Each row of Fig. A1 represents one pair, divided into their respective quasars. The spectra, displayed in the rest frame as a black curve, are modelled with the best-fitting solution in blue, which includes components such as continuum emission (orange), iron emission (cyan), narrow emission lines (green), and broad emission lines (red). The sections used for fitting continuum emission are indicated by gray bars at the top of the panel. For the quasar pair J2209, we used the host spectral decomposition method described by Ren et al. (2024). In J0847 and J1214, significant segments of the spectra fall below 3500 Å, where quasar emission prevails. For J1416, the spectra, merged from long-slit and IFU observations, present challenges in ensuring a consistent host contribution across the spectral range. Meanwhile, for J2337, the host's impact is minimal, which is supported by the galaxy fraction obtained from image decomposition (Table 1). However, it is important to note the potential overestimation of the black hole mass due to the host's influence on $L_{\lambda}(5100\text{Å})$ in these analyses. Residuals from the spectral fitting (data minus model) appear as gray dashed lines at the bottom. Given the study's primary focus, we concentrated on fitting the broad emission lines and their related narrow lines, with these regions highlighted in the bottom sub-panels for each source. Further technical details on PYQSOFIT can be found on its Github page[4] and in Guo et al. (2019).

The analysis provides the width of each emission line and the monochromatic luminosity at specific wavelengths. The monochromatic luminosity of 5100 Å (L_{5100}, column 5) is used to derive the bolometric luminosity ($L_{\rm bol}$, column 6), using a correction factor of 9.26 as stated in Richards et al. (2006). The broad emission lines, specifically MgII, Hβ, and Hα, are used in the virial approach to determine the masses of BH (Vestergaard & Peterson 2006; Schulze et al. 2018). These measurements are recorded in Table A1, columns (7–9). The measurement uncertainties are minor compared to the systematic uncertainties of the virial methods, which are approximately 0.4 dex, as reported by Shen et al. (2011); Shen (2013); Schulze et al. (2018). Subsequently, the Eddington luminosity ($L_{\rm Edd}$) and the Eddington ratio ($\log\ \lambda_{\rm Edd}$) are computed as:

$$L_{\rm Edd} = 1.26 \times 10^{38} M_{\rm BH}$$
$$\lambda_{\rm Edd} = L_{\rm bol}/L_{\rm Edd} \quad \text{(A1)}$$

[4]https://github.com/legolason/PyQSOFit/tree/master

We compare the PYQSOFIT fitting results of the broad emission lines and decide the best to use (in bolder fonts among columns 7–9) for $\lambda_{\rm Edd}$ (column 10).

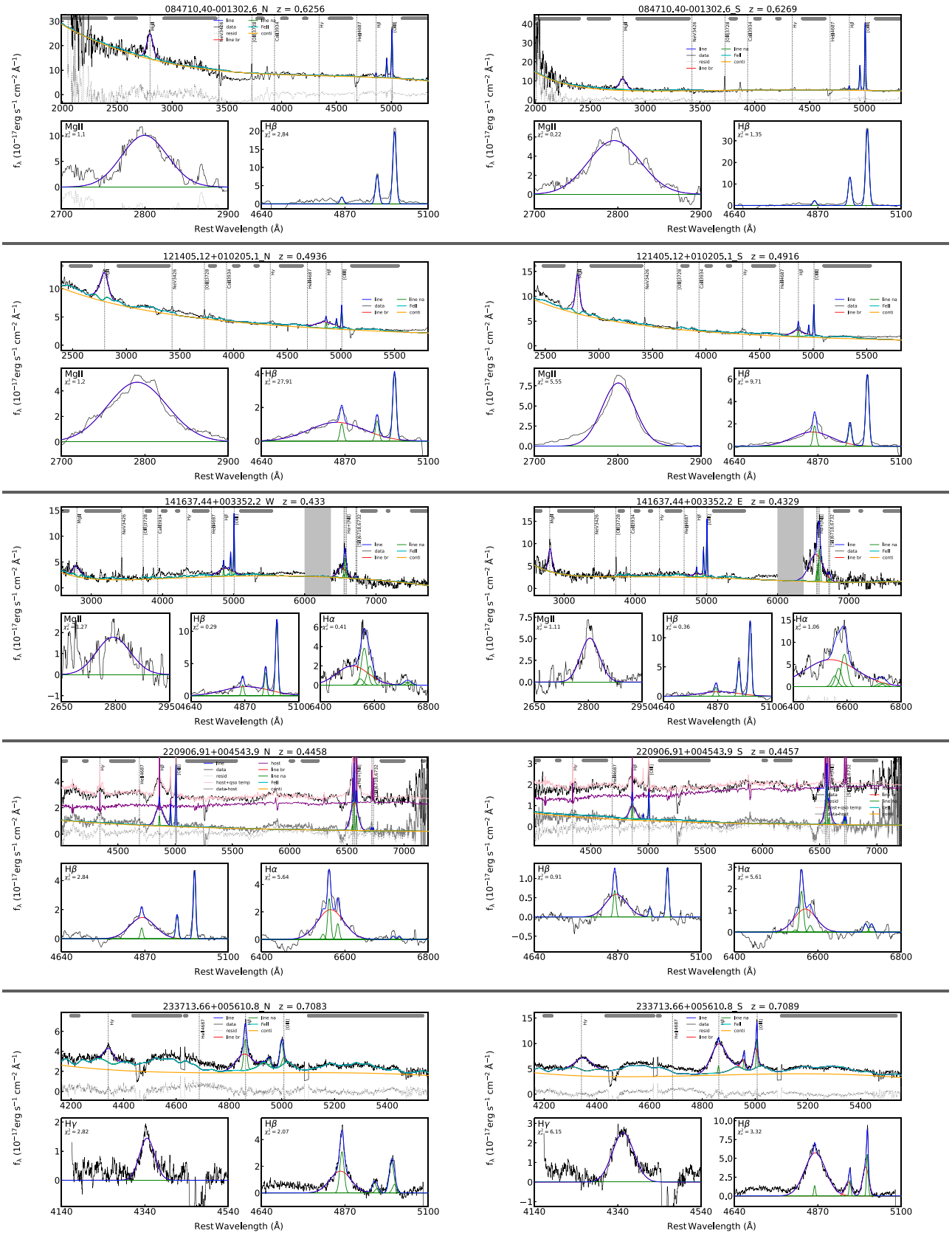

Figure A1. PyQSOFit analysis of the five dual quasar systems. Each row represents a pair, divided into two components. For each component, the upper sub-panel displays the full spectrum, along with the optimal fit model, including broad and narrow emission lines, iron emission, and continuum emission. The lower sub-panel provides a close-up of the broad emission line composites, with χ^2 values indicated at the top left.

Table A1. Updated BH characteristics of the dual quasars with PYQSOFIT.

Name	RA (hh:mm:ss)	Dec. (dd.mm.ss)	z	$\log \lambda L_\lambda(5100\text{Å})$ (erg s^{-1})	$\log L_{\rm bol}$ (erg s^{-1})	$\log M_{\rm BH}^{\rm Mg\,II}$ ($M_\odot$)	$\log M_{\rm BH}^{\rm H\beta}$ ($M_\odot$)	$\log M_{\rm BH}^{\rm H\alpha}$ ($M_\odot$)	$\log \lambda_{\rm Edd}$
(1)	(2)	(3)	(4)	(5)	(6)	(7)	(8)	(9)	(10)
J0847N	08:47:10.402	−00:13:02.460	0.6256	44.73	45.61	**8.92**	–	–	−1.42
J0847S	08:47:10.440	−00:13:03.288	0.6269	44.62	45.4	**8.77**	–	–	−1.48
J1214N	12:14:05.110	01:02:07.188	0.4936	44.11	45.04	**8.83**	9.05	–	−1.90
J1214S	12:14:05.134	01:02:05.028	0.4916	43.88	44.87	**8.25**	8.64	–	−1.49
J1416W	14:16:37.418	00:33:52.416	0.433	43.72	44.52	9.10	9.07	**8.89**	−2.48
J1416E	14:16:37.459	00:33:52.200	0.4329	43.77	44.63	8.43	–	**8.34**	−1.82
J2209N	22:09:06.912	00:45:43.848	0.4458	43.29	44.26	–	**7.97**	7.88	−1.82
J2209S	22:09:06.900	00:45:42.228	0.4457	42.98	43.95	–	**7.66**	7.53	−1.82
J2337N	23:37:13.694	00:56:12.048	0.7083	44.33	45.3	–	**8.15**	–	−0.97
J2337S	23:37:13.673	00:56:10.752	0.7089	44.61	45.58	–	**8.47**	–	−1.00

Columns (2–3): Central locations of the point sources obtained from the HSC *i*-band imagery. These locations are indicated by the white crosses in Fig. 3.
Column (4): Spectroscopic redshift of the sources determined by PYQSOFIT.
Column (5): Monochromatic luminosity at 5100 Å (L_{5100}) derived from power-law continuum fitting. The uncertainties in L_{5100} are negligible with 200 MC samplings in PYQSOFIT, as the power law's shape is reliably constrained.
Column (6): Bolometric luminosity ($L_{\rm bol}$) of the quasars calculated using monochromatic luminosity L_{5100} and a bolometric correction factor of $\rm BC_{5100} = 9.26$ as per Richards et al. (2006); Shen et al. (2011).
Column (7-9): BH mass ($M_{\rm BH}$) assessed using the virial method with broad Mg II (Schulze et al. 2018), H β (Vestergaard & Peterson 2006), and H α lines (Schulze et al. 2018), respectively.
Column (10): Eddington ratio ($\lambda_{\rm Edd}$). The $M_{\rm BH}$ employed for this calculation is emphasized in bold in columns 7–9.

This paper has been typeset from a TEX/LATEX file prepared by the author.